

**Fabrication of High-Quality Microflexures  
Using Micromilling Techniques**

by

Joshua B. Gafford

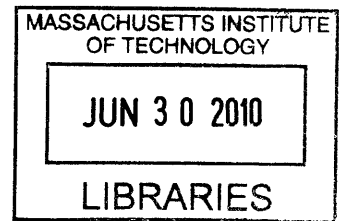
Submitted to the Department of Mechanical Engineering  
in Partial Fulfillment of the Requirements for the Degree of  
Bachelor of Science in Mechanical Engineering

at the

Massachusetts Institute of Technology

June 2010

**ARCHIVES**



© 2010 Massachusetts Institute of Technology  
All rights reserved

Signature of Author.....

*Joshua B. Gafford*  
Department of Mechanical Engineering  
May 10, 2010

Certified by .....

*Martin L. Culpepper*  
Martin L. Culpepper  
Associate Professor of Mechanical Engineering  
Thesis Supervisor

Accepted by .....

*John H. Lienhard V*  
John H. Lienhard V  
Coombs Professor of Mechanical Engineering  
Chairman, Undergraduate Thesis Committee



# **Fabrication of High-Quality Microflexures Using Micromilling Techniques**

by

Joshua B. Gafford

Submitted to the Department of Mechanical Engineering  
on May 10, 2010 in Partial Fulfillment of the  
Requirements for the Degree of Bachelor of Science in  
Mechanical Engineering

## **ABSTRACT**

This research focuses on the feasibility of using micromilling as a process for fabricating the flexural body of mesoscale nanopositioners. A desire to fabricate non-silicon microflexures for more favorable material properties and flexural responses has led MIT's Precision Compliant Systems lab to investigate the use of various metals in the design of mesoscale six-axis HexFlex nanopositioners. Micromilling is being sought as an alternative method of manufacturing HexFlex flexural bodies due to its inherent process and material flexibility. Cutting forces were approximated (and verified using FEM and previously-measured results) in order to select cutting parameters that would avoid tool failure and ensure workpiece integrity. Several HexFlex devices were successfully micromilled from various aluminum alloys. Total machining time, including setup and tool changes, was around 1.5 hours per part. The integrity of each part was verified using optical microscopy and white-light interferometry to inspect for any microcracks or otherwise unfavorable by-products of the milling process. Ultimately, it was shown that micromilling is a feasible process for manufacturing low-volume to-spec mesoscale nanopositioners ( $\pm 3 \mu\text{m}$ ) with surface roughnesses of less than  $0.300 \mu\text{m}$ . Process improvements are suggested based on observations before and during the machining process.

Thesis Supervisor: Martin L. Culpepper  
Title: Associate Professor of Mechanical Engineering

## **Acknowledgments**

I would like to thank Professor Martin Culpepper for offering me the opportunity to work on such a unique project. His enthusiasm for my work and persistent feedback greatly facilitated my passion for this research.

I would also like to thank Robert Panas for answering my pesky questions and providing invaluable feedback throughout the duration of my research.

Finally, and most importantly, I would like to thank my parents for their continued love and support throughout my academic career. In the interest of sounding as clichéd as possible, without them, none of this would have been possible.

## **Table of Contents**

Abstract.....	3
Acknowledgements.....	4
Table of Contents.....	5
List of Figures.....	7
List of Tables.....	9
Chapter 1: Introduction.....	10
Chapter 2: Background.....	11
2.1 Background on Flexural Mechanisms.....	12
2.2 Background on Micromilling.....	13
2.3 Coalescence of Micromilling and Microflexure Fabrication.....	13
Chapter 3: Theory/Modelling.....	13
3.1 Idiosyncrasies of the Micromilling Process.....	14
3.2 Cutting Parameters.....	15
3.3 Cutting Force Estimation.....	16
3.4 Avoiding Tool Failure.....	20
Chapter 4: Machining Parameter Selection.....	25
4.1 Selection of Cutting Parameters.....	25
4.1.1 Spindle Speed and Cutting Feed Rate.....	25
4.1.2 Depth of Cut.....	27
4.2 Strategies for Machining Thin Features.....	28
4.3 Strategies for Optimizing Surface Finish.....	29
Chapter 5: Case Study: Machining HexFlex.....	30
5.1 Toolpath Generation.....	31
5.2 Hardware Preparation.....	34
5.3 Machining.....	35
Chapter 6: Results, Observations, and Suggestions for Process Improvement.....	37
6.1 Use of Coolant.....	38
6.2 Effects of Vibration.....	39
6.3 Fixturing.....	40
6.4 Dimensional Precision.....	42

6.5 Surface Roughness Measurements.....	43
6.6 The Future: Scaling Down.....	47
Chapter 7: Conclusion.....	48
References.....	50
Appendix A.....	54
Appendix B.....	57

## **List of Figures**

<b>Figure 1(a):</b> Solid model of silicon-based HexFlex.....	10
<b>Figure 1(b):</b> Micromilled Aluminum 6061-T6 HexFlex .....	10
<b>Figure 2:</b> Schematic of axial depth-of-cut versus radial depth-of-cut.....	15
<b>Figure 3:</b> Polynomial fit for material coefficient $K_m$ of Aluminum 6061.....	17
<b>Figure 4:</b> Correlation between theoretical cutting forces and measured cutting forces.....	18
<b>Figure 5:</b> 2-D orthogonal cutting model used in FEM simulations.....	19
<b>Figure 6:</b> Correlation between theoretical cutting forces and FEM.....	19
<b>Figure 7:</b> Microscopic images of failed micro-endmills.....	21
<b>Figure 8:</b> Simplified state-of-stress within tool under cutting loads.....	22
<b>Figure 9:</b> Recommended spindle speed and feed rates based for vs. tool diameter.....	26
<b>Figure 10:</b> Recommended chip load and material removal rates vs. tool diameter.....	26
<b>Figure 11:</b> Plot of theoretical surface finish dependence.....	30
<b>Figure 12(a):</b> Microlution 363-S 3-axis horizontal micro-milling machine.....	31
<b>Figure 12(b):</b> View of micromill working area with callouts for important features.....	31
<b>Figure 13:</b> Toolpath generation, solid verification and process descriptions.....	33
<b>Figure 14(a):</b> Shim stock, sacrificial fixture, micromill pallet.....	35
<b>Figure 14(b):</b> Fixture and pallet assembly.....	35
<b>Figure 14(c):</b> Stock, fixture and pallet assembly.....	35
<b>Figure 15(a):</b> Initial facing operation (6061-T6).....	37
<b>Figure 15(b):</b> Initial pocket-clearing passes (1100).....	37
<b>Figure 15(c):</b> Final contour pass (1100).....	37
<b>Figure 16(a):</b> HexFlex machined from Al 6061-T6 with initial facing operation.....	38
<b>Figure 16(b):</b> HexFlex machined from Al 1100 shim stock.....	38
<b>Figure 17:</b> Microscopic images of HexFlex machined without liquid coolant.....	39
<b>Figure 18:</b> Microscopic images of flexural blade, showing vibration-induced roughness.....	40
<b>Figure 19:</b> Web shearing phenomenon during initial facing operation.....	41
<b>Figure 20:</b> Improved fixturing system, with kinematically-locating pegs and screw clamps...	42
<b>Figure 21:</b> Run chart of measured blade thickness vs. specified.....	43
<b>Figure 22:</b> Interferometer imaging locations.....	44
<b>Figure 23:</b> Experimental setup for white light interferometer measurements.....	44

**Figure 24:** Sample surface maps produced by the interferometer..... 45  
**Figure 25:** Measured surface roughness vs. theoretical surface roughness..... 46  
**Figure 26:** Measured surface roughness data for four 7075 Al HexFlex Devices..... 47  
**Figure B-1:** Spec sheet of Microlution 363-S 3-axis horizontal micro-milling machine..... 54  
**Figure B-2:** Fully-dimensioned part drawing for sacrificial fixture..... 55  
**Figure B-3:** Test part for roughly quantifying minimum blade and web thickness..... 56



**List of Tables**

**Table 1:** Process parameters for HexFlex machining..... 31

**Table 2:** Process parameters for experimentally determining minimum rib & web thickness... 48

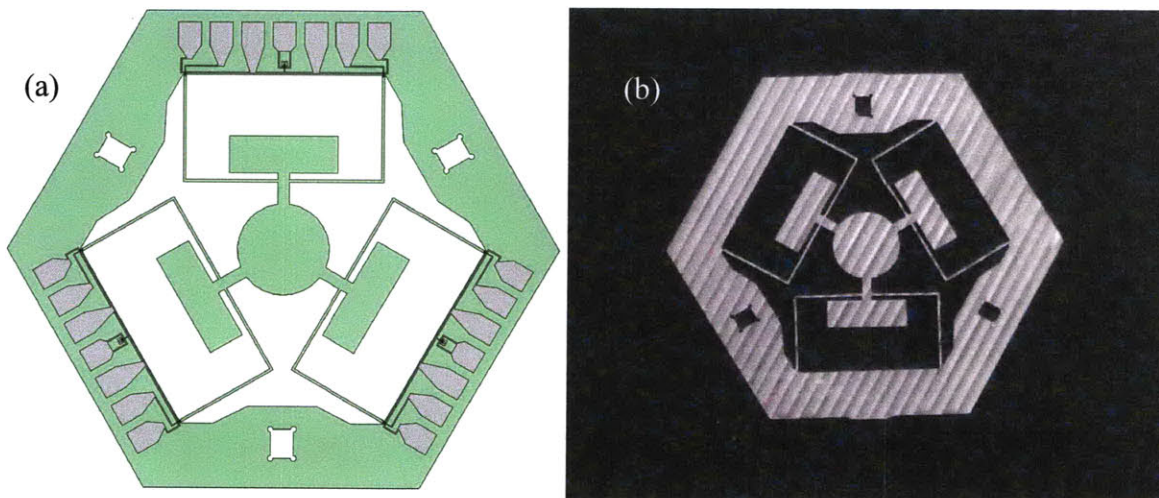
**Table B-1:** Measurements of blade thickness..... 56

**Table B-2:** White-light interferometer surface roughness measurements..... 57

## Chapter 1: Introduction

This research aims to generate the knowledge required to prototype high-quality microflexures using micromilling. Currently, microflexures are fabricated using conventional lithographic microfabrication processes. Micromilling is a promising alternative to conventional fabrication techniques given the greater design and material flexibility associated with the process. Micromilling would make it feasible for designers to rapidly prototype MEMS components in small batches for research, testing and validation purposes due to the low overhead cost of prototyping. The current MEMS spectrum is dominated by silicon-based devices due to manufacturing limitations. The material flexibility offered by micromilling opens up a new design space with regards to materials selection, making it feasible for designers to build larger-scale and more robust structures.

This thesis describes the first step required to rapidly prototype MEMS devices outside of conventional microfabrication processes. A case study is presented in which micromilling was used to manufacture a meso-scale six-axis flexural nanopositioner called HexFlex, developed by MIT's Precision Compliant Systems Laboratory. The HexFlex is approximately 4 cm in diameter and has features as small as 200  $\mu\text{m}$ . A solid model and a micromilled HexFlex are shown in Figure 1(a) and 1(b).



**Figure 1:** (a) Solid model of silicon-based HexFlex nanopositioner, showing the electrical traces for Lorentz actuation, and (b) a micromilled Al 6061-T6 HexFlex

Machining parameters were selected based on simple cutting force models to avoid tool failure and ensure part integrity. These models were validated through finite element analysis and previously-obtained empirical results. A Microlution 363-s 3-axis CNC micromill was used to fabricate HexFlex devices from several aluminum alloys. Optical microscopy and white-light interferometry were used to quantify surface finish and investigate the finished parts for any microcracks, evidence of vibration, and other by-products of the machining process. The accuracy and precision of the micromilling process were quantified within a 95% confidence envelope using statistical methods, and it was found that the micromill upholds dimensional tolerances as small as  $\pm 3$  microns. Additionally, the surface roughness of several parts was measured for different cutting parameters and found to be less than 300 nm in all cases.

Chapter 2 provides a background of flexural mechanisms and the micromilling process in order to validate the relevance of this research. Chapter 3 presents the theoretical modeling of cutting forces and toolpiece stresses that dictated the selection of machining parameters. Chapter 4 describes the approach taken to select cutting parameters and describes the rationale behind their selection. Chapter 5 gives an account of the machining process, and Chapter 6 presents observations of the machining process and the results of microscopy and white-light interferometer measurements. Chapter 7 concludes the paper with an overview of the takeaways of this research, and offers suggestions for future research and validation.

## **Chapter 2: Background**

As the world becomes increasingly focused on miniaturization, MEMS (Micro Electro-Mechanical Systems), or “factories on a chip,” are seeing exponential growth and development in industry and academia alike. Flexural based compliant mechanisms are often used in MEMS technology as precision manipulators because of their ability to exhibit linear kinematic behavior and experience low hysteresis [1]. Microflexural positioners have widespread applications, from confocal imaging to nanometrology to precision machining. MIT’s Precision Compliant System’s Laboratory (PCSL) has developed a six-axis nanopositioner called HexFlex to address the growing need for high-precision compliant manipulators.

Due to manufacturing constraints at such small characteristic length scales, the great majority of MEMS components are fabricated from silicon using lithography. PCSL has been investigating the fabrication of such components out of metals (aluminum and steel) to take

advantage of superior material properties and the potential for less-costly manufacturing processes. Currently, the HexFlex manufacturing process costs about \$35,000, and requires anywhere from 6 months to a year to manufacture a new prototype.

The present research focuses on validating the plausibility of moving the fabrication of the flexural body to the micromill. Micromilling will add flexibility to the production of MEMS components by moving the manufacturing process outside of traditional microfabrication. Due to the relatively low overhead cost of micromilling, it would be an attractive alternative for designers seeking to prototype components in a small batch environment. Additionally, it opens up a different design space with regards to material selection.

### *2.1 Background on Flexural Mechanisms*

In order to validate the relevance of this research, it is useful to understand what flexural nanopositioners are and how they are applicable to high-precision MEMS. Flexural mechanisms make use of material strain to effectively eliminate backlash and produce motion in a kinematic, predictable manner. Flexures typically consist of a rigid positioning stage that undergoes translation as allowed by the flexural members (characteristically thin members). Flexures are designed to permit motion in a desired actuation direction, and prohibit motion in undesired directions. PCSL has developed a mathematical method of analyzing flexural systems known as Freedom and Constraint Topology (FACT). FACT theory provides a designer with a methodical means of designing flexure-based systems based on desired degrees of freedom and degrees of constraint. See Reference [2] for more information on FACT methodology.

At the MEMS level, a system of metrology is often integrated into the flexural mechanism to characterize the motion of the flexure and permit closed-loop control. Typical actuation methods for flexural nanopositioners include thermomechanical (deformation of flexural members by resistive heating) and capacitive actuation (deformation of flexural members by electrostatic repulsion).

Flexural performance is highly dependent on the material properties (Young's modulus, strain rate, Poisson's ratio) of the flexural members. A desire to expand the material catalog for nanopositioner fabrication, thus opening up a wider array of possible material properties and flexural responses, necessitates manufacturing processes outside of traditional microfabrication methods used to produce silicon MEMS components.

## 2.2 *Background on Micromilling*

Micromilling is seeing increasing exposure in the fabrication of miniature components such as microdies, molds, biomedical devices and MEMS components due to its lower cost, flexibility, and material compatibility. Coupled with sophisticated CAM software, micromilling produces complex 3-dimensional topographies with the precision of a few microns. A drawback of micromilling is the slow material removal rate that limits productivity and adds cost to machined parts. The typically low initial overhead cost and process flexibility make micromilling an ideal manufacturing alternative for designers looking to quickly and inexpensively prototype high-quality components.

## 2.3 *Coalescence of Micromilling and Microflexure Fabrication*

Prior literature searches have turned up no evidence of any research being done regarding the appropriation of micromilling to the manufacturing of microflexures. The basic function of microflexures is to allow translation in a specified direction through the deformation of thin flexural members, so one may imagine how restraining these members and avoiding workpiece yield might be a problem in the presence of stresses induced by mechanical material removal methods. Current methods of fabricating metallic flexural bodies at PCSL include wire-EDM, which uses chemical reactions to remove material as opposed to mechanical material removal characteristic of conventional machining methods. Wire-EDM necessitates pre-drilling of wire entrance holes, is incapable of machining slotted features with dimensions of 50 microns (~0.002 inches) or smaller, and is not very economical for low-volume prototyping due to initially high overhead costs. Due to its negligible overhead, as well as process and material flexibility, micromilling could be an ideal solution for designers wishing to prototype new designs in a small-batch environment.

## **Chapter 3: Theory/Modelling**

In order to intelligently select machining parameters that will avoid tool failure and optimize part integrity, it is important to gain a basic understanding of the theory involved in micromilling processes. Equations presented hereafter are simplified in nature when compared to more complex micromilling cutting models [3-4], but the intent is to create a quick way of estimating

relevant cutting forces at an order-of-magnitude level in order provide a rational foundation for the selection of machining parameters.

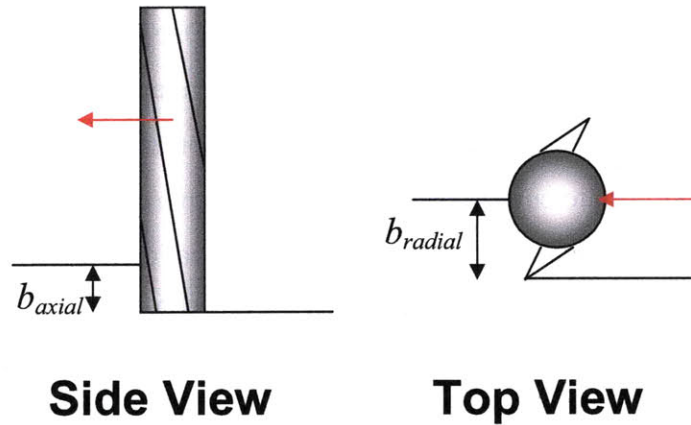
### 3.1 *Idiosyncrasies of the Micromilling Process*

Several studies have been performed in an effort to understand how micro end-milling operations (MEMO) differ from conventional end-milling operations (CEMO). Although kinematically the processes are similar, a so-called “size effect” occurs at the micro-level that results in a much higher ratio of feed-per-tooth to radius of the cutter that will ensure reasonable material removal rates (MRR’s). Current manufacturing methods are incapable of fabricating tungsten-carbide end-mills with sharp edges due to limitation of structural strength of the tool by way of stress concentrations at the edge [5]. As a result, cutting edge radii at the MEMO level are proportionally larger than those in CEMO tools. Additionally, as tools get smaller, their decreased stiffness leads to greater tool deflection which compromises the dimensional accuracy of the workpiece. Thermal effects are much more pronounced and lead to residual stresses and unfavorable deformation on the cutting face of the tool. Due to the size effect, micro-endmills are much more susceptible to abrupt changes in processing parameters (stepovers, rapid decreases/increases in chip load) due to mechanical and thermal shock. If cutting parameters and toolpaths are not selected intelligently, the life of micro-tools is shortened drastically and the surface integrity of the workpiece is compromised. In micromachining, there is no audible signature to suggest that the tool has been broken during cutting; as a result, valuable time could potentially be lost if tool failure is not detected.

Unlike CEMO, there are no handbooks available for the selection of cutting parameters for MEMO operations. If one were to consult the *Machinery’s Handbook* while machining aluminum 6061-T6 with a 100 micron end-mill, he would find that the required spindle speed is ~350,000 RPM, which is clearly difficult to achieve in practice [6]. As a result, one cannot simply consult *Machinery’s Handbook* to calculate machining parameters prior to machining a part. In order to provide logical grounds for the selection of cutting parameters, both theoretical and empirical results will be correlated in an attempt to lay out a general guide for selecting cutting parameters for MEMO operations.

### 3.2 Cutting Parameters

Although modern CAM software enables machinists to control numerous aspects of the milling process, the scope of this report is confined to selection of four parameters that characterize most basic milling operations: spindle speed  $N$  [RPM], cutting feed rate  $f_c$  [mm/min], axial depth of cut  $b_{axial}$  [mm] and radial depth of cut  $b_{radial}$  [mm]. The difference between axial and radial depths-of-cut is illustrated in Figure 2.



**Figure 2:** Schematic of axial depth-of-cut versus radial depth-of-cut

Tool selection gives rise to three more parameters that will be used in subsequent calculations: tool diameter  $d$  [mm], flute length  $l_{flute}$  [mm] and number of flutes  $Z$ . Given  $N$  and  $f_c$ , the *chip load* (or alternatively, feed-per-tooth)  $f_t$  [mm/tooth] may be calculated as follows:

$$f_t = \frac{f_c}{NZ} \quad (1)$$

The following sections in this chapter will present a simplified mechanical analysis of the involved cutting forces and their impact on the tool. Relevant factors of safety will be calculated that will allow for the selection of  $N$ ,  $f_c$  and  $b$  that will avoid tool failure and maximize material removal rates:

$$MRR = d \cdot b \cdot f_c \quad (2)$$

It will be shown in subsequent sections that, unlike in CEMO, chip load may not be held constant for a specific part material across the spectrum of available MEMO tool diameters due to limitations in spindle design and tool manufacturing. Chip load decreases substantially with a decrease in tool diameter, which invariably leads to very small material removal rates.

### 3.3 Cutting Force Estimation

Calculating relevant cutting forces in the milling process is useful for intelligently selecting cutting parameters that will maximize tool life and avoid tool failure. Additionally, knowledge of the relative magnitudes of cutting forces is useful when machining thin elements, such as flexural blades, in order to predict whether or not the thin member will significantly deflect or yield during nominal cutting conditions. Bao and Tansel have proposed a complex analytical cutting force model that accurately estimates the instantaneous feed and normal cutting forces as functions of tool angle  $\theta$  to within a 5% error envelope [3]. One should consult this model for an extremely accurate analysis of the cutting force and its dependence on tool angle. In a machine-shop setting, it is more useful to come up with a general, order-of-magnitude force estimation with which to select appropriate cutting parameters. For the purpose of this research, the cutting force  $F$  was approximated to be a function of chip load  $f_t$ , axial depth of cut  $b_{axial}$  and a “material coefficient”  $K_m$  that is an empirically-determined value. Dimensional analysis shows the relationship to be as follows:

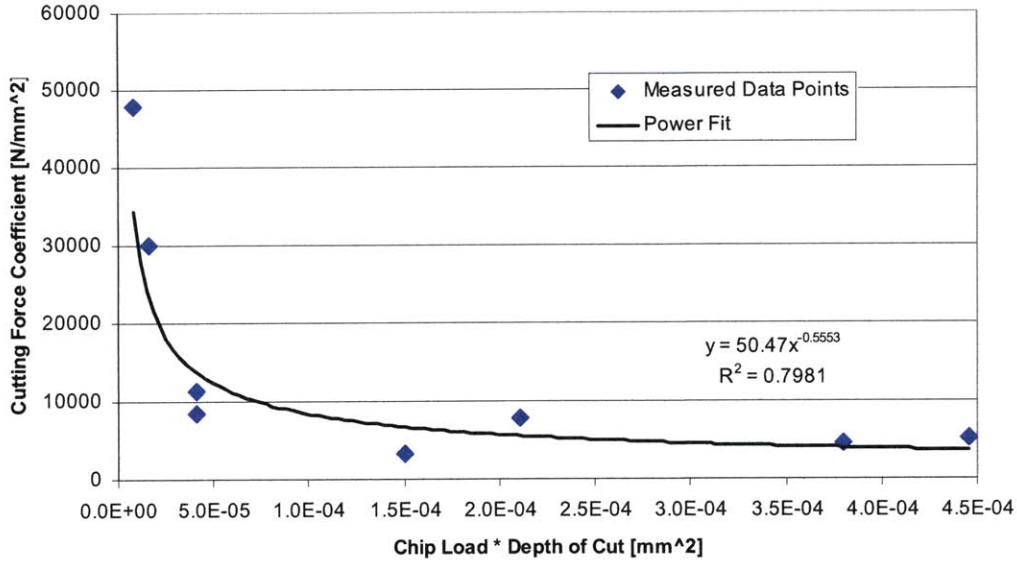
$$F_c = f\left(K_m \left[\frac{N}{\text{mm}^2}\right], b_{axial}, [\text{mm}], f_t, [\text{mm}]\right) \quad (3)$$

$$\Pi_1 = \text{Constant} = \frac{F_c}{K_m \cdot b_{axial} \cdot f_t} \quad (4)$$

$$\therefore F_c = \text{Constant} \cdot K_m \cdot f_t \cdot b_{axial} \quad (5)$$

The material coefficient  $K_m$  is both material and process dependent. The constant is a by-product of dimensional analysis and may be used to roughly scale the cutting forces to other materials. Ziegert et al. performed several tests to estimate  $K_m$  for Aluminum 6061 using Bao and Tansel’s analytical cutting force model [7]. Figure 3 shows the dependence of  $K_m$  on the product of  $f_t$  and  $b$  for Aluminum 6061 using the results obtained by Ziegert et al.





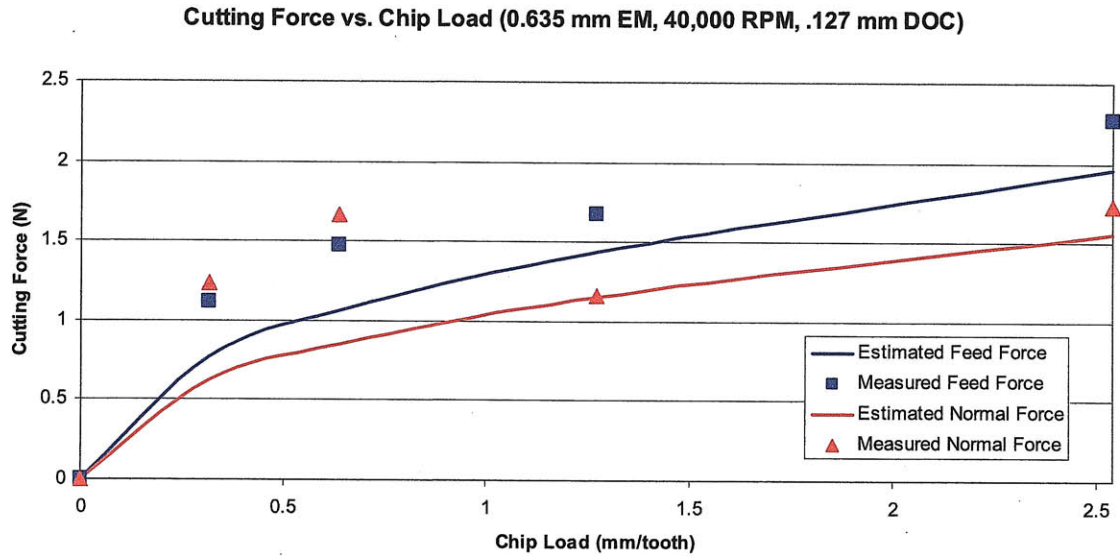
**Figure 3:** Polynomial fit for material coefficient  $K_m$  of Aluminum 6061

Using the power fit obtained from Ziegert's results, one may quickly approximate the cutting forces that a tool experiences during nominal operating conditions by inputting  $f_t$  and  $b$  specific to the process. In Ziegert's case the constant is 1, as it is the constant about which the constants for other materials are normalized. A review of literature found that the cutting force estimation in Equation 5 may be scaled to other aluminum alloys roughly by the ratio of the shear strength of the workpiece to that of Aluminum 6061. This is somewhat intuitive, as the primary mode of resistance against the cutting tool during operation is the shear resistance of the workpiece over the primary shear plane where chip formation is generated. Equation 5 may be modified:

$$F_c \approx \left( \frac{\tau_y^{workpiece}}{\tau_y^{6061}} \right) 50.47 \cdot (f_t \cdot b_{axial})^{.445} \quad (6)$$

Equation 6 was used to calculate the cutting force in both the normal and feed directions. A review of literature found the ratio of feed force to normal force to be slightly less than unity (between 0.6 and 0.8) so this factor was taken into account during calculations. The axial force due to part springback was ignored for reasons of conservative estimation; this force compresses the tool and actually alleviates the stresses induced from bending and torsion. Figure 4 shows a comparison of theoretical cutting forces using Equation 6 with estimated average measured cutting force values from graphs produced by Dhanorker and Özel for Al 2024-T6

( $\tau_y^{2024-T6} / \tau_y^{6061} \approx 1.36$ ) [8]. As Figure 4 suggests, Equation 6 offers a relatively suitable order-of-magnitude cutting force estimate which is sufficient for the purposes of this research.

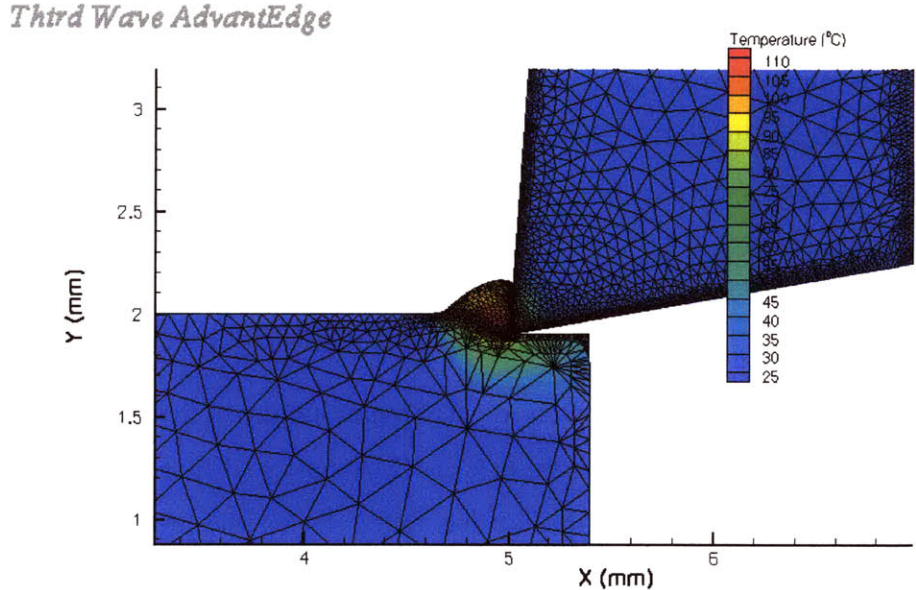


**Figure 4:** Correlation between theoretical cutting forces calculated from Equation 6 and those measured by Dhanorker et al.

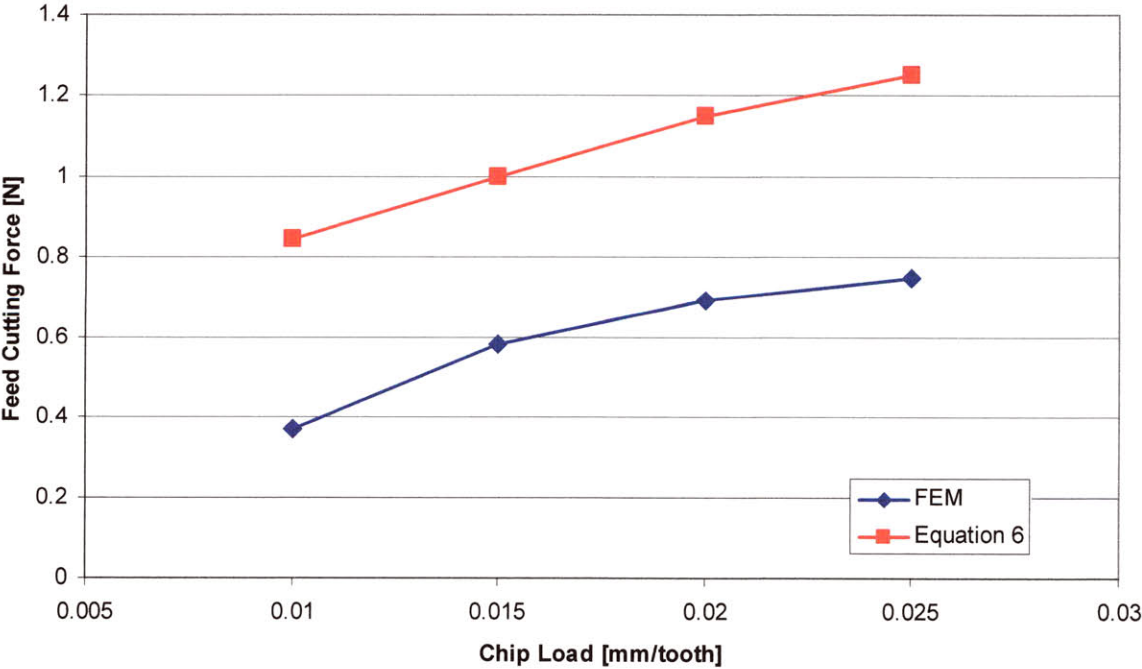
In order to further validate the cutting force approximation derived in Equation 6, *AdvantEDGE* finite element method software was used to estimate cutting forces given certain process parameters and material properties. This software treats the micromilling process as a 2-dimensional orthogonal cutting model to approximate cutting forces, stresses, and temperatures throughout the tool and the workpiece. A screenshot of the *AdvantEDGE* viewport is shown below in Figure 5.

Due to the extremely fine meshing algorithm used, simulations take upwards of two hours to reach steady state results. In the interest of both time and computer resources, a few simulations were run at various chip loads, and the maximum average cutting force was extracted and correlated with the cutting force predicted by Equation 6 under identical cutting conditions. The results of this correlation are shown in Figure 6. Figure 6 shows that theoretical forces generated from Equation 6 are about a factor of two larger than those predicted by FEM. Comparing Figures 4 and 6, the theoretically-determined cutting forces fall somewhere between measured

results and FEM predictions, so from an order-of-magnitude standpoint, Equation 6 seems to give an adequate cutting force estimation.



**Figure 5:** 2-D orthogonal cutting model used in AdvantEdge FEM software.

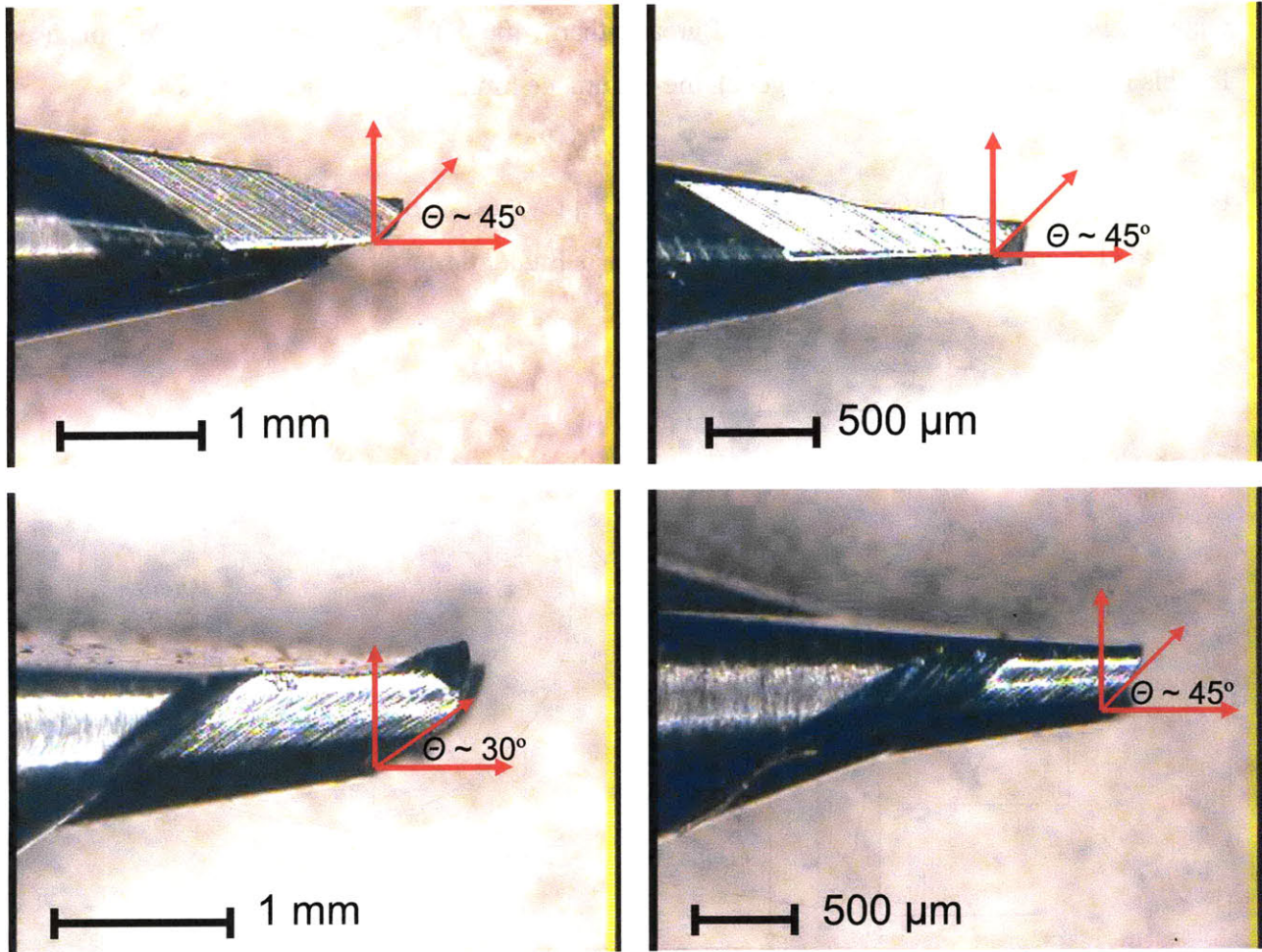


**Figure 6:** Correlation between theoretical cutting forces calculated from Equation 6 and those predicted using finite element method

It must be reiterated that this approximation is purely mechanical and is only valid for aluminum. Micromilling is an extremely complex process wherein dynamic and temperature effects play a relatively significant role as well. Additionally, tool runout was neglected, and if significant, may affect both the cutting forces and the achievable precision. The scope of this research is limited to machining HexFlex devices using aluminum, and Equation 6 is a conservative estimate, useful for identifying the state of stress within the toolpiece in a benchtop setting. Cutting force estimates generated with Equation 6 are comparable with measured results in several previous studies.

### *3.4 Avoiding Tool Failure*

At the microscale, tools often undergo catastrophic failure at the tool root as opposed to edge failure which is commonly experienced in CEMO. A survey of four different tools (Performance Micro Tools tungsten carbide end-mills) that failed during the process of machining HexFlex shows this to be the case, as they all failed at the tool root and the majority failed at an angle of  $45^\circ$  from the axis of the tool. A  $45^\circ$  fracture plane indicates either brittle failure in torsion or ductile failure in tension. Since tungsten carbide is inherently brittle, it is likely that these tools failed in torsion due to the orientation of the fracture plane. The torsional stress is due to the distributed feed cutting force on the cutting edge of the end mill. Figure 7 shows microscopic images of the failed tools.



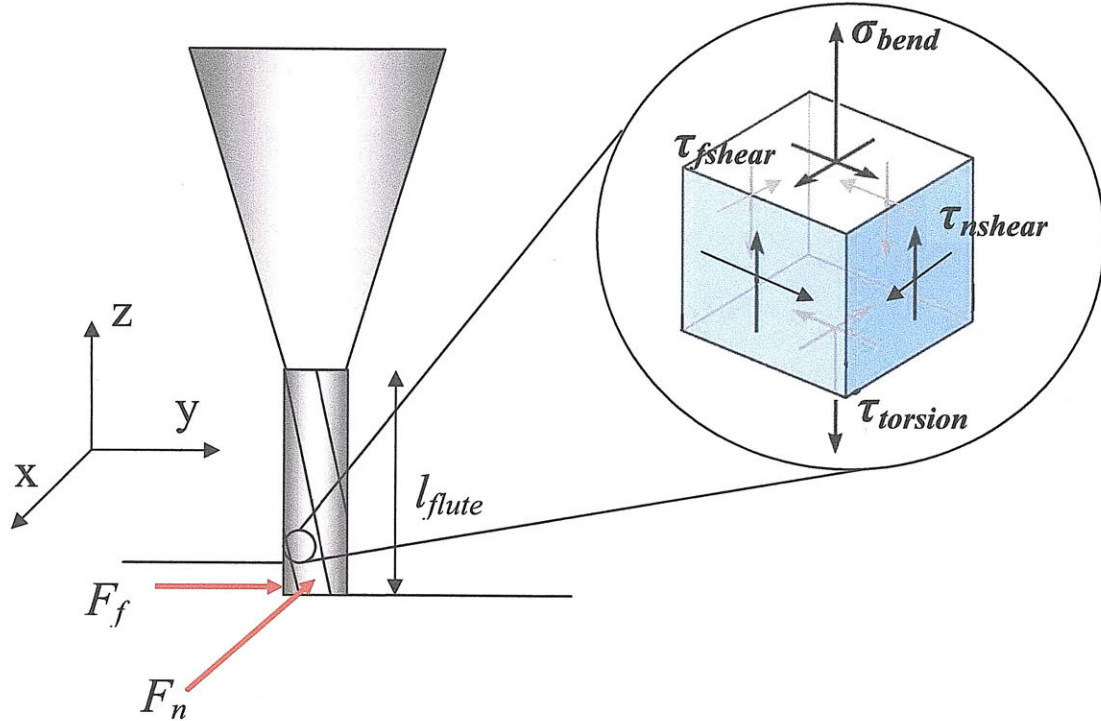
**Figure 7:** (clockwise from top left) 508  $\mu\text{m}$  (0.020") end mill, 381  $\mu\text{m}$  (0.015") end mill, 508  $\mu\text{m}$  (0.020") end mill, 1016  $\mu\text{m}$  (0.040") end mill

MEMO tool failure is either instantaneous or fatigue-driven. Instantaneous failure is experienced when the cutting force from workpiece to tool imparts a state of localized stress within the tool that exceeds the yield stress of the tool material. Fatigue-driven failure is the result of exposure to numerous loading/unloading cycles. Even though the instantaneous state of stress within the toolpiece is less than the yield stress, the repeated application and removal of this stress fatigues the material and causes failure over time by the generation and propagation of microcracks. Loading cycles on tools in end-milling operations are sinusoidal in nature and cycle between a maximum and minimum cutting force. To avoid fatigue, it is recommended that the maximum cutting forces never exceed the forces allowed by the stress endurance limit of the tool

material. For steels with yield stresses of greater than 1400 MPa (the tungsten carbide tools used for this research fall under this category), the endurance limit may be approximated as:

$$S_e = 700 \text{ MPa} \quad (7)$$

Based on the cutting force relations given in the previous section, the state of stress within a material element in the toolpiece is approximated as Figure 8 illustrates.



**Figure 8:** Simplified model of cutting forces on tool, showing the state-of-stress in a material element

The bending stress  $\sigma_{bend}$  is orientation-dependent; for the purpose of subsequent calculation it will be the stress induced by the maximum of the cutting forces. The action of the feed force against the cutting edge (offset from the neutral axis of the tool) induces a torsional shear component  $\tau_{torsion}$ . Finally, since the tool is short ( $d_{tool} = (1/3)l_{flute}$ ), shear effects from the normal and feed forces ( $\tau_{nshear}$  and  $\tau_{fshear}$ ) become significant as well. The fundamental equations for the four stresses considered in this analysis are given in Equations 8-11.

$$\sigma_{bend} = \frac{d_{tool} F_{feed} l_{flute}}{2I} \quad (8)$$

$$\tau_{torsion} = \frac{8F_{feed}}{\pi \cdot d_{tool}^2} \quad (9)$$

$$\tau_{fshear} = \frac{16F_{feed}}{3\pi \cdot d_{tool}^2} \quad (10)$$

$$\tau_{nshear} = \frac{16F_{normal}}{3\pi \cdot d_{tool}^2} \quad (11)$$

Here,  $I$  is the second moment of area of the tool. Due to the complex geometric cross-sections of end-mills,  $I$  was calculated as a function of an *effective diameter*, which is the diameter of a uniform cylinder that exhibits the same bending characteristics as the end mill (the effective diameter is estimated as  $0.8 \cdot d_{tool}$ ). Thermally induced stresses are neglected, as they are mostly confined to the tool tip, far away from where mechanical stresses are maximized. The corresponding Cauchy stress tensor is as follows:

$$\bar{\sigma} = \begin{bmatrix} 0 & \tau_{torsion} & \tau_{nshear} \\ \tau_{torsion} & 0 & \tau_{fshear} \\ \tau_{nshear} & \tau_{fshear} & \sigma_{bend} \end{bmatrix} \quad (12)$$

Stresses are maximized at the interface of the fluted region and the tapered shoulder, as this is where internal moments and shear forces are the greatest. For the purpose of this research, only failure in this region is considered. As failure in microtools is predominately brittle, stress invariants are used to find the principal stresses and then Mohr's brittle failure criterion is applied to gauge whether or not the tool is likely to fail immediately given the cutting forces. The principal stresses are characterized by the roots of the following equation:

$$\sigma^3 - I_1\sigma^2 + I_2\sigma - I_3 = 0 \quad (13)$$

The invariant constants in the simplified microtool model are:

$$I_1 = \sigma_{bend} \quad (14)$$

$$I_2 = -(\tau_{fshear}^2 + \tau_{nshear}^2 + \tau_{torsion}^2) \quad (15)$$

$$I_3 = 2 \cdot \tau_{fshear} \tau_{nshear} \tau_{torsion} - \sigma_{bend} \tau_{torsion}^2 \quad (16)$$

Once the three principal stresses are identified, it is possible to calculate toolpiece factors of safety (FOS) based on the cutting forces, which are functions of the cutting parameters.

As an added safety measure, one should add a stress concentration proportionality factor  $K_s$  to account for any mechanisms of fast fracture in the tool, such as imperfections in the material structure of the tools (microstructural voids, cracks) and the stress concentrations that accompany the sharp angle between cutting flutes and the inner diameter of the end mill. A stress concentration factor of 2 is suitable for the cutter geometry (historically, a concentration factor of 3 is used in the presence of spherical voids in the microstructure, so this value may be used as an extremely conservative estimate) [9].

The principal stresses from Equation 13 were used to calculate safety factors for instantaneous and fatigue-driven failure based on Mohr's brittle failure criterion and Goodman fatigue criterion for cyclic loading, respectively. A program was generated in MathCAD that was used to help select cutting parameters on the fly. The spreadsheet and the equations used to generate results are left to Appendix A for brevity. Given input cutting conditions (tool diameter, spindle speed, axial and radial depth of cut, and feed speed), the spreadsheet conservatively estimates immediate and fatigue-driven FOS to help determine whether or not too much stress is being put on the toolpiece given the cutting conditions. Building a program or spreadsheet is a useful practice that helps to take the guesswork out of cutting parameter selection on the fly.

The above analysis is for selecting cutting parameters that will avoid instantaneous tool failure. Wear effects on the cutting edge are of interest as well with regards to part integrity. A commonly accepted metric with which to predict the life of a tool is the Taylor equation, which relates the life of the tool  $T$  to the cutting speed  $V$ :

$$VT^n = C \quad (17)$$

where  $n$  and  $C$  are material constants. Previous studies [10] have shown that spindle speed is the most significant detriment to tool life, and depth of cut has a negligible effect. Additionally, it has been shown that increasing the chip load actually increases tool life (with respect to wear on the cutting edge), yet an increased chip load also increases the cutting forces which invariably leads to fatigue failure if the forces exceed those allowed by the endurance limit of the tool material. One should consult the aforementioned reference [10] for a more in-depth study of wear patterns on the cutting edge as a function of cutting parameters. At the microscale, temperature effects become significant; the higher  $f/r_{edge}$  ratio and faster cutting speeds lead to significant temperature gradients on the tool face that negatively impacts the longevity of the



tool. Use of fluid coolant is greatly preferred and highly advantageous with regards to temperature moderation on the cutting edge.

## **Chapter 4: Machining Parameter Selection**

### *4.1 Selection of Cutting Parameters*

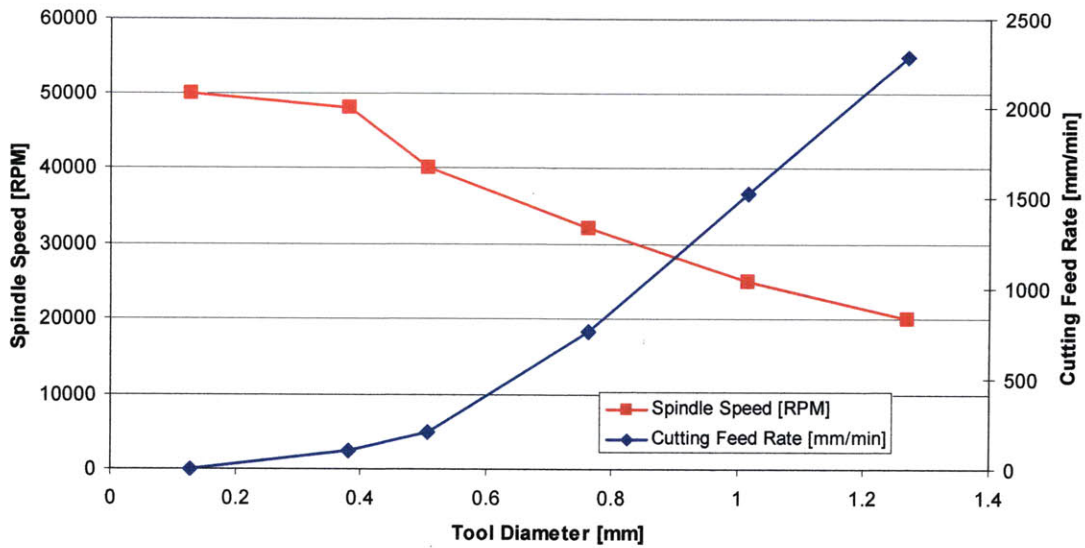
Now that the state of stress in a toolpiece during nominal cutting conditions has been conservatively approximated, the cutting parameters may be selected. Cutting parameters should be selected to maximize MRR and minimize the possibility of tool failure by keeping the cutting forces within predefined limits.

#### **4.1.1 Spindle Speed and Cutting Feed Rate**

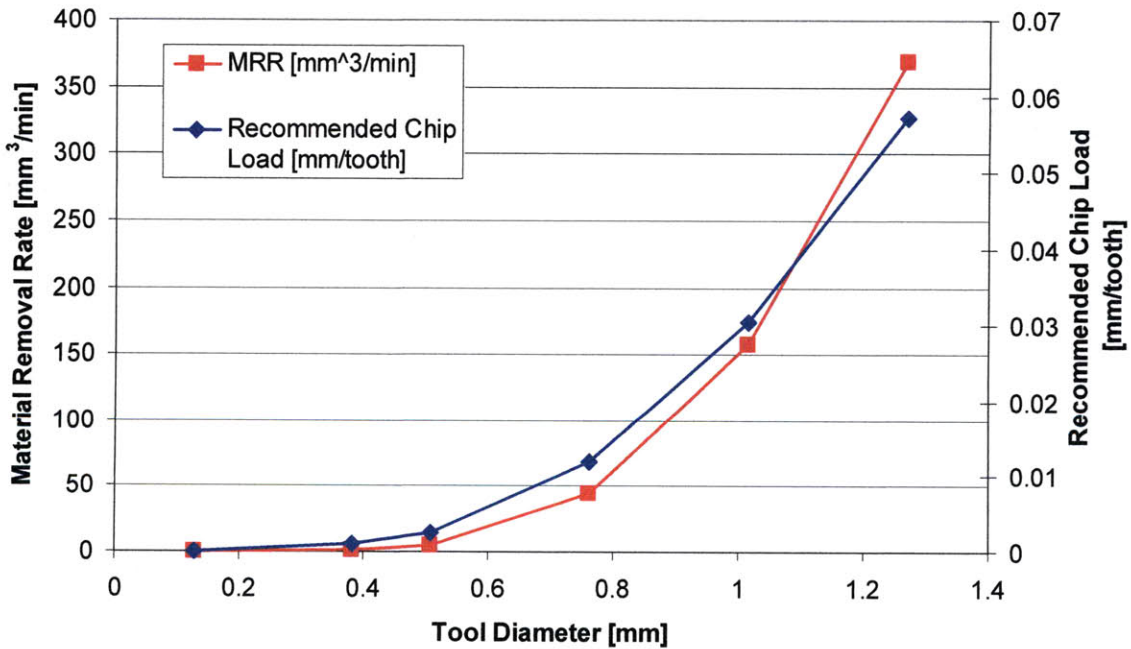
As mentioned previously, extrapolating CEMO spindle speeds to the micro level is not always practical, as this methodology might necessitate spindle speeds of >100,000 RPM for smaller tools which is difficult to achieve in commercial spindles. As micromilling has a higher  $f_z/r$  ratio, selection of spindle speed and cutting feed is a coupled process; the quotient of the two ultimately determines the chip load. Recalling the Equation 1, one may constrain the chip load on the cutting edge (thereby constraining the allowable cutting force based on the state of stress within the tool) by increasing spindle speed and decreasing the cutting feed rate.

The graph shown in Figure 9 shows recommended spindle speeds and cutting feed rates as a function of tool diameter (that keep the fatigue factor of safety above 1; note that this is extremely conservative) for cutting Aluminum 6061. This graph is based purely on the analytical stress model derived in Chapter 3. The depth of cut is held at  $1/10^{\text{th}}$  tool diameter for reasons explained in the next section.

It should be noted that the recommended speeds and feeds shown in Figures 9 and 10 are those for which the associated stresses induced on the tool are less than the endurance limit of the tool material with a stress concentration factor of 3. One must also be wary of the surface finish; the faster the feed rate and the slower the spindle speed (the greater the chip load), the greater the surface roughness. A polynomial relationship between surface roughness, chip load and surface speed will be presented in *Section 4.5*.



**Figure 9:** Recommended spindle speed and feed rates based on conservative stress fatigue model for Al 6061-T6 (stress concentration factor  $K_s=3$ )



**Figure 10:** Recommended chip load and material removal rates vs. tool diameter, based on conservative stress fatigue model for Al 6061-T6 (stress concentration factor  $K_s=3$ )

Figure 9 shows that as tool diameter decreases, the feed rate must decrease proportionally with the increase in spindle speed rate to maintain a chip load below limits set by the endurance

strength of the tool material. It must also be noted that recommended chip load increases exponentially with larger tools, not linearly as one might be inclined to think. Note that there is a spindle speed cap at 50,000 RPM, as this is the upper speed limit for the machine that the HexFlex devices were micromilled on. For tools with diameters of 200 microns and below, recommended feed rate is on the order of 1 – 10 mm/min, which results in extremely low material removal rates. From a production standpoint, larger tools should be used to clear out the bulk of the material in pocket operations, and the smaller tools should be reserved for finishing contour operations. Given the relatively low cost of microtools (~\$50.00 for end mills less than 127  $\mu\text{m}$  or 0.005” in diameter), it might be more economical to operate with cutting forces greater than those specified by tool endurance limit in order to increase MRR at the risk of tool breakage. Obviously this is process-dependent and ultimately under the discretion of the machinist.

#### **4.1.2 Depth of cut**

Depth of cut selection is a non-trivial process. On the one hand, as the depth of cut increases, the cutting force exerted on the tool by the workpiece increases, thereby increasing the possibility of tool wear and breakage. On the other hand, too shallow of a cut will result in ploughing, where the surface of the workpiece deforms elastically under the loading of the tool and fails to produce a chip. Therefore, the minimum depth of cut is defined by a minimum undeformed chip thickness required to successfully yield the workpiece along the primary shear plane. Kim et al [12] found that the minimum chip thickness is on the order of 1/4<sup>th</sup> the radius of curvature of the cutting edge. As typical cutting edge radii for microtools are on the order of a few microns, this restriction is relatively insignificant at the mesoscale level.

A rule of thumb is to set the maximum roughing axial depth of cut to 1/10<sup>th</sup> the diameter of the toolpiece to ensure a compromise between low cutting forces, material removal rate and surface finish. The maximum finishing stepdown should be 50%-75% the roughing depth of cut. These values allow for reasonable spindle speed selections based on the maximum allowable stress in the toolpiece. For face-milling operations, superior surface finish is achieved by decreasing the radial depth of cut during the finishing process. Any face-milling operations used in machining HexFlex used a radial depth of cut of  $d_{\text{tool}}/2$  at the finishing level.

## 4.2 Strategies for Machining Thin Features

HexFlex nanopositioners are designed to be compliant in certain directions while restricting motion in other directions. Recalling Figure 1, the presence of thin (200  $\mu\text{m}$ ) blades leads to non-trivialities with respect to machining. If improperly restrained, the normal component of the cutting force and the periodic loading/unloading nature of the cutting process could lead to deformations/vibrations in thin members far away from their connecting point to stiffer, non-compliant members. This leads to an undesirable surface finish, burr formation and imprecision as the part deflects under the cutting load and less material is removed.

Specific to HexFlex, the Euler-Bernoulli beam bending equation is used to approximate how much deflection the thin feature will undergo when exposed to normal cutting forces:

$$\delta_{blade} = \frac{F_n L_{blade}^3}{18EI} \quad (18)$$

where  $E$  is the modulus of elasticity of the workpiece material and  $I$  is the second moment of area of the blade cross-section. Equation 17 assumes that the central positioning stage is infinitely stiff in relation to the thin flexural blades, and compressive compliances are neglected. The maximum deflection scales with  $F_n$  and with  $1/t^3$ . During toolpath generation, an approach to mitigate deflection is to decrease the radial cutting depth while milling the outside contours of these blades. In doing so, one benefits from both decreased normal cutting forces and increased blade thickness during each pass that withstands these cutting forces. Given a typical normal finishing cutting force of  $\sim 0.1$  N and inputting the geometry of the blade (400  $\mu\text{m}$  thick, 200  $\mu\text{m}$  wide, maximum length of 9.32 mm), the maximum deflection during a finish cut is roughly 243  $\mu\text{m}$  (FEA simulations show a max deflection of 239  $\mu\text{m}$  under similar loading conditions)! As this is well outside the acceptable tolerance range, methods of restraining the deflection of thin features under loading are required to uphold dimensional precision.

Another issue that might arise when machining thin members is resonance. If the loading/unloading cycles on the workpiece from the tool match the natural frequency of the workpiece geometry, vibratory excitation is induced that drastically affects surface finish and precision. Natural frequency of a thin beam is estimated as:

$$\omega_n = \sqrt{\frac{k}{m}} \quad (19)$$

where  $k$  is the bending stiffness of the member and  $m$  is the mass. For loads induced by the normal cutting force component, Equation 17 results in a resonant frequency of around 570 Hz for HexFlex. Finite element simulations have shown that the first three modes of vibration for HexFlex occur around 400 Hz. As micromilling necessitates spindle speeds between 10,000 RPM and 50,000 RPM (166 Hz – 833 Hz), unrestrained vibration could very well become an issue. As a result, methods must be employed to secure thin members and avoid significant mechanical deformation and vibration under load.

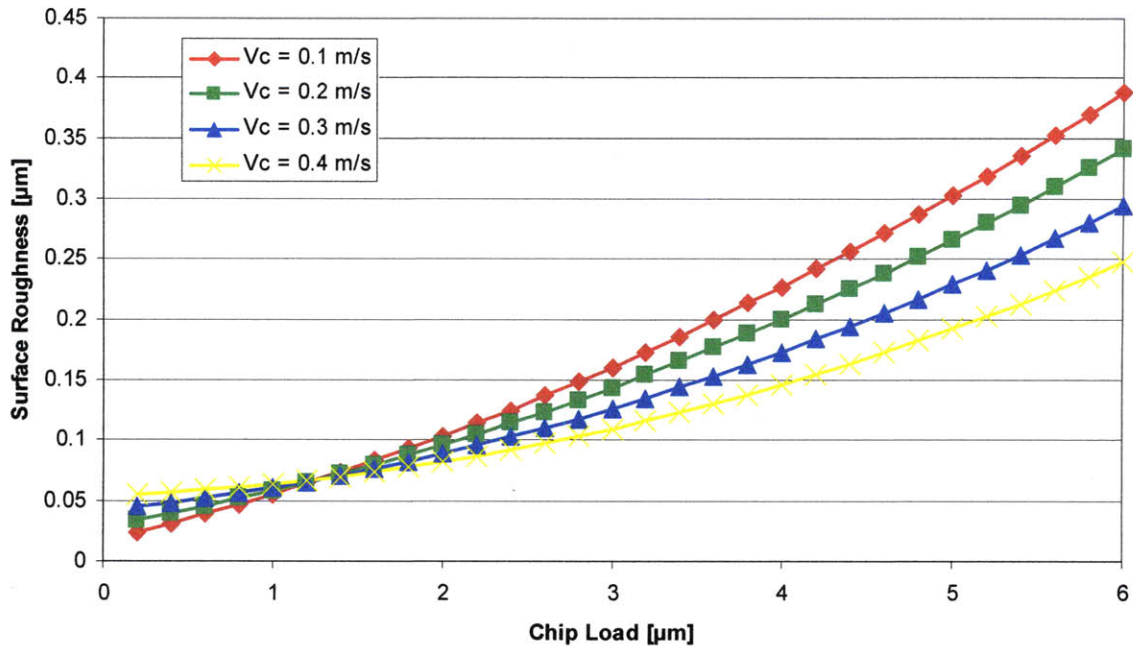
The current method employed to avoid thin-member deflections is to use an adhesive to secure these thin members to the fixture. The shear resistance of the adhesive helps to secure the thin members and prevent any significant deformation. Additionally, the viscous nature of the adhesive helps to dampen out any resonances or vibrations that might be excited within the workpiece.

#### 4.3 *Strategies for Optimizing Surface Finish*

Due to its scale, MEMO prohibits burr removal during post-machining processes. Therefore it is imperative that cutting parameters be selected so as to minimize burr formation and maximize surface finish. Lee and Dornfeld [13] performed several tests with aluminum to quantify a relationship between surface roughness, chip load and cutting speed; it was found that the relationship is non-linear and follows the polynomial fit in Equation 20:

$$R_a = 43.6 + 439f_t + 46.3f_t^2 + 1256v_c - 990f_tv_c \quad (20)$$

where  $f_t$  is measured in  $\mu\text{m}$ ,  $v_c$  is surface speed measured in m/s, and  $R_a$  is measured in Angstroms. The polynomial fit is shown in Figure 11, where the units of  $R_a$  have been converted to  $\mu\text{m}$ .



**Figure 11:** Plot of theoretical surface finish dependence

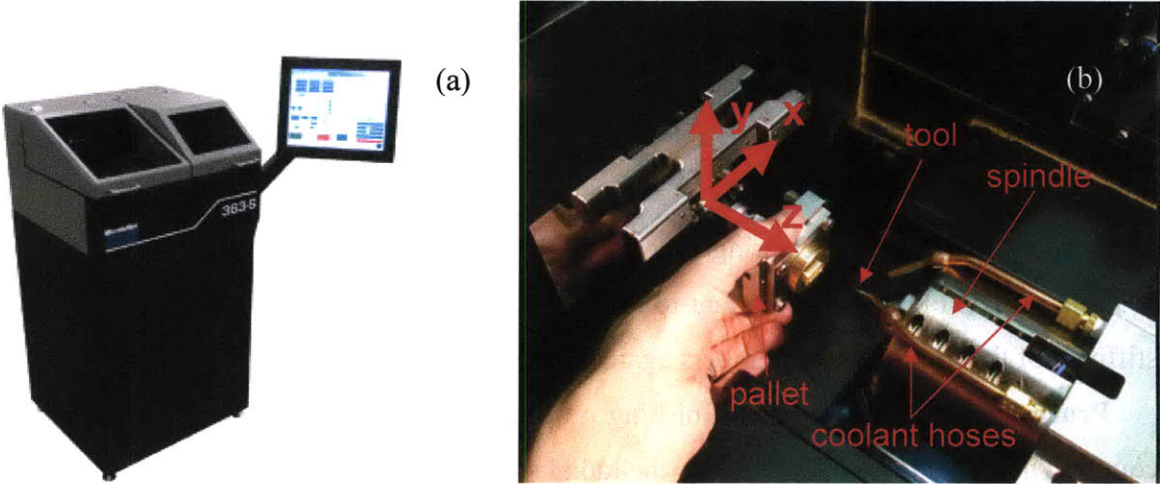
It is both intuitive and evident from Figure 11 that surface roughness increases with increased chip load and decreased cutting speed. As the cutting feed (and accordingly the chip load) is decreased, the tool spends more time over the workpiece and has more opportunity to remove material, thus decreasing the surface roughness. Decreasing the chip load has the most significant impact on surface quality; at around 1  $\mu\text{m}$  chip load, the surface roughness is roughly constant despite cutting speed. Many dynamic factors influence surface finish, and the validity of Equation 18 specific to HexFlex manufacturing will be investigated in a subsequent section.

Although this wasn't practiced in the face-milling of the 6061-T6 Aluminum, climb cuts should be employed exclusively at finishing levels if optimum surface finish is desired over the added feed plane traversal time.

## Chapter 5: Case Study: Machining HexFlex

The cutting parameters selected via theoretical models derived in Chapter 3 were employed to machine HexFlex nanopositioners in two ways: (1) from 1 mm thick Aluminum 6061-T6 sheet stock, and (2) from 0.015" thick Aluminum 1100 shim stock. The HexFlex devices were

cut using Microlution 363-S 3-axis horizontal micro-milling machine, shown in Figure 12. The spec sheet for the mill is in the appendices.



**Figure 12:** (a) Microlution 363-S 3-axis horizontal micro-milling machine, (b) view of working area with coordinate system and callouts for important features

5.1 Toolpath Generation

Toolpaths for HexFlex were generated in HSMWorks, a CAM software package developed by Dassault Systems. The entire machining operation consists of five different processes that necessitate the use of three different tools. The process parameters for each path are shown in Table 1. Additionally, sequential pictures of each toolpath as well as respective solid verifications are shown in Figure 13.

**Table 1:** Process parameters for HexFlex machining

Process	Toolpiece Diameter [mm]	Spindle Speed [RPM]	Cutting Feed [mm/min]	Axial DOC [mm]	Radial DOC [mm]	Final Depth [mm]	Machining Time [min:sec]
1	3.175	12,000	254	0.30	1.50	-.5525	13:55
2	1.016	36,000	229	0.15	0.96	-.9525	16:58
3	0.381	50,000	127	0.06	0.381	-.9525	28:12
4	3.175	12,000	254	0.30	3.175	-.9525	3:16

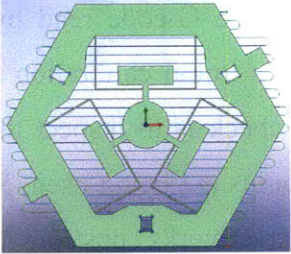
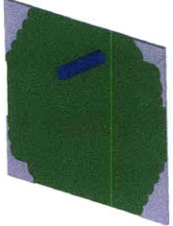
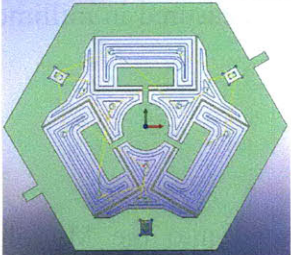

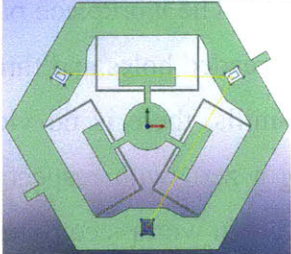

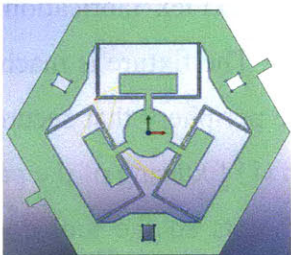

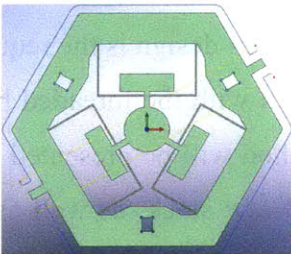

**Process 1** is only necessary if the stock material being used is thicker than the specified thickness of the final part. It is a facing operation that reduces the raw stock thickness to the final thickness of the part. HSMWorks does this automatically, but facing stepovers should nominally be curved or radial so as to ensure constant chip load on the tool and prevent abrupt loading variations that lead to tool failure. Additionally, the maximum stepover distance is set at half of the tool diameter (1.5 mm) to decrease chip load, thereby increasing surface finish as per Equation 18.

**Process 2** is a pocket clearing process to remove the bulk of the material from the interior contours of HexFlex. It is important to leave about ~0.5 mm of radial stock for added structural stiffness of the thin flexural members against the normal component of the cutting force.

**Process 3** and **Process 4** are finishing processes that clean up the interior contours and the coupling holes. This process removes the radial stock left over from Process 3, but uses a smaller tool diameter and lighter chip load to decrease the cutting forces and minimize deflections in the thin members. It is good practice to use climb-cuts on finishing processes when end-milling contour features, as climbing cuts result in a much cleaner surface finish.

**Process 5** cuts out the outside hexagonal contour, leaving two 2 mm thick tabs to restrain the part to the uncut stock during the final cuts. These tabs are removed with a razorblade once machining has completed.



Toolpath Generation	Solid Visualization	Process Description
		<p><b>Process 1*:</b> Face-Milling down to specified HexFlex Thickness. Zero Z at top of stock, machine to max depth of <math>d_1 = -(t_{stock} - t_{spec})</math>.</p>
		<p><b>Process 2:</b> Pocket clearing interior contours. Leave ~0.5mm of radial stock to increase stiffness of thin flexural members against normal cutting forces. Machine through part (Set top of stock = <math>-(t_{stock} - t_{spec})</math>, machine to depth of <math>d_2 = -t_{stock}</math></p>
		<p><b>Process 3:</b> Finishing out peripheral coupling holes. Same depth parameters as Process 2.</p>
		<p><b>Process 4:</b> Finishing out interior contours. If corner radii are of concern, select tool diameter that will create tolerable fillet radius. Same depth parameters as Process 2.</p>
		<p><b>Process 5:</b> Cutting out external hexagonal contour. Same depth parameters as Process 2.</p>

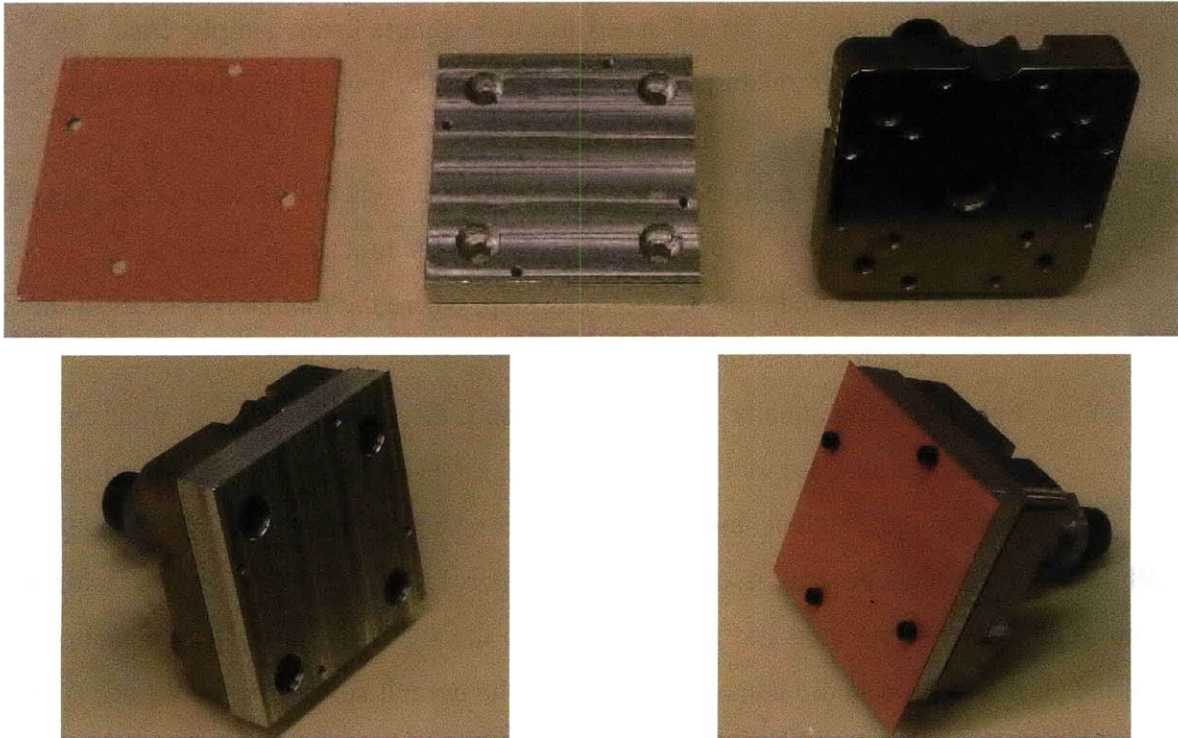
**Figure 13:** Toolpath generation, solid verification and process descriptions

\* Recall that Process 1 is not required if machining from shim stock at HexFlex’s specified thickness. Machining begins with Process 2, where Z is zeroed at top of stock and max depth is  $-t_{spec}$

Once the toolpaths are generated for each operation, they are post-processed using Microlution's Beaverworks post-processor. Post-processing generates the G-code read by the micro-mill, and the Beaverworks post-processor automatically includes initial calibration steps required by the Microlution mill. Prior to machining, a good sanity check is to inspect the G-code in HSMWorks Edit and make sure the correct tools, zeros, and units are being used. Some familiarity with basic G-code commands is highly recommended. Beaverworks' post-processor automatically uses the millimeter as its base unit (coordinate system is measured in millimeters, feed rates are in mm/min).

## 5.2 *Hardware Preparation*

After toolpaths have been generated, post-processed and uploaded into the Microlution control panel, it is necessary to prepare the hardware prior to machining. The workpiece pallets for the micromill are simply flat, planar hardened steel surfaces with threaded holes and through holes for mounting custom fixture pieces. Unlike conventional end-mills, there is no vice to quickly secure parts and no edge-finding/zeroing process to specify a zero with respect to a desired datum surface on the workpiece. As a result, one must be creative in workpiece fixturing. For this research, a sacrificial fixture was developed specifically for HexFlex fabrication that screws onto the micromill pallet via four 10-32 socket-head cap screws. The fixture is machined out of 6061-T6 Aluminum and has four 4-40 threaded holes lining the periphery that secure the piece of raw stock to the fixture. This fixture performs two main tasks: (1) fixturing of the part to the pallet, and (2) providing a (soft) sacrificial material for through-cuts so the tool doesn't contact the pallet, thus avoiding breakage. A fully-dimensioned drawing of the sacrificial fixture is in the Appendices for future reference. An unfortunate by-product of this design is the required pre-machining of the raw stock with four 4-40 through-holes that align with the threaded holes on the sacrificial part. A suggestion for a more efficient fixturing method will be presented later in this paper. Figures 14(a)-(c) show the pallet, sacrificial piece, and raw stock, as well as the order of assembly. The sacrificial part is secured to the pallet via the 10-32 cap screws. A layer of adhesive (double-sided tape) is applied to the sacrificial part to dampen vibration of the thin flexural blades during machining, and the stock is secured to the sacrificial part via the 4-40 cap screws that fixture the stock against the relatively large cutting forces present in initial facing and clearing operations.



**Figure 14:** (a) (from left) shim stock, sacrificial fixture, micromill pallet, (b) fixture and pallet assembly, (c) stock, fixture and pallet assembly

When designing custom fixtures and cutting stock to size, it is important to note that the top of the fixture and stock must remain flush with the top surface of the pallet. A tool calibration laser lies just above the top plane of the pallet, and any interference with this laser will inevitably lead to errors in tool zeroing.

### 5.3 Machining

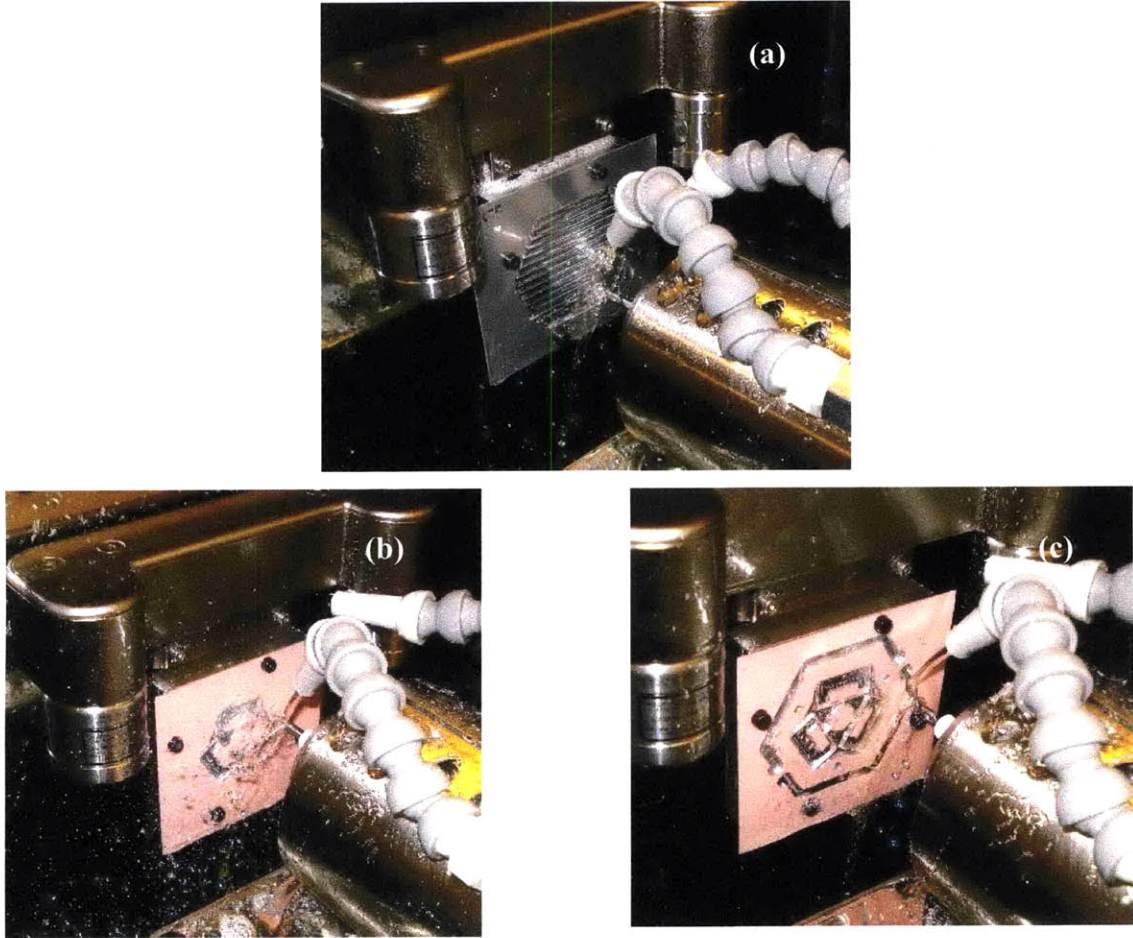
The entire machining process is summarized in the following numbered steps:

- 1) Boot up Microlution GUI
- 2) Setup – Phase Motors
- 3) Combine – Browse (Locate G-Code) – Add to Queue – Load
- 4) Unclamp Pallet (if pallet gets stuck, open pressure regulator to ~85 psi)
- 5) Take out placeholder, insert new pallet – Clamp Pallet
- 6) Release Tool – take out placeholder tool, insert new tool – Clamp Tool

- 7) Enable Spindle – Start (If asked to clear spindle error, simply click “OK” and Start again. If problem persists, disable spindle, rewind G-code and click “Start” again)
  - a) The first motion is a calibration step, where the tool undergoes rapid motion to a calibration laser to locate the tool tip.
  - b) The second motion is zeroing step, where the tool slowly feeds in the Z to touch off the top of stock
- 8) Spindle automatically retracts in Z and disengages when a tool change is necessary. Release tool – insert new tool – Clamp tool, and push Start to continue machining. The machine automatically re-calibrates after each tool change.

While the machining process is underway, the Microlution GUI allows the machinist the freedom to alter the cutting feed and spindle speed on the fly. This allows for manual override capabilities in response to audio cues from the tool. The default spindle speed setting is 10,000 RPM, and the GUI doesn't always automatically update in response to spindle speed callouts from the G-code. As an added safety measure, the machinist should manually set the appropriate spindle speed during calibration steps when the tool is not engaged in the workpiece.

The initial facing operation necessary to machine the Al 6061-T6 stock is shown in Figure 15(a). Pictures of the machining process for a HexFlex being machined out of 1100 shim stock are shown in Figures 15(b) and 15(c). The entire machining time, including setup time and tool changes, was about ~1.5 hours.



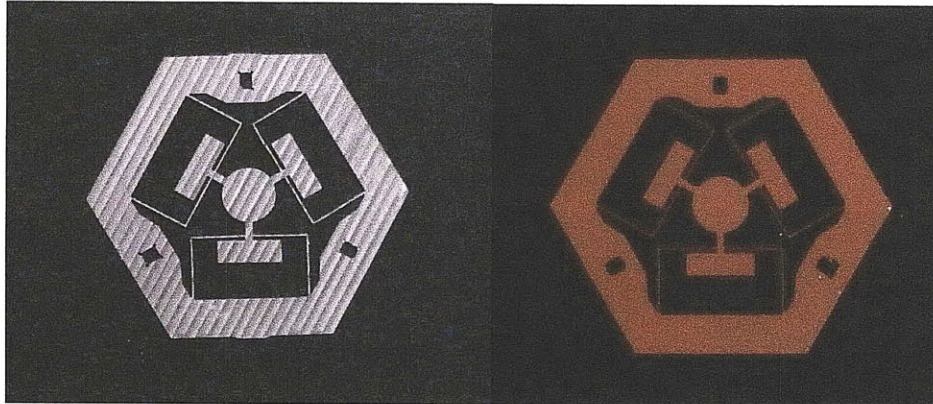
**Figure 15:** (a) Initial facing operation (6061-T6), (b) Initial pocket clearing passes (1100)  
(c) final contour pass (1100)

After machining has completed, the pallet is removed from the mill and the part is carefully removed from the pallet by unscrewing the 4-40 screws and sliding a razorblade between the fixture and the part to remove the layer of adhesive. The restraining tabs are then cut off with the razorblade and filed down if necessary.

## **Chapter 6: Observations and Suggestions for Process Improvement**

The finished HexFlex devices are shown in Figure 16. Given a visual inspection of each flexure, the quality seems very comparable to the silicon version in terms of dimensionality.

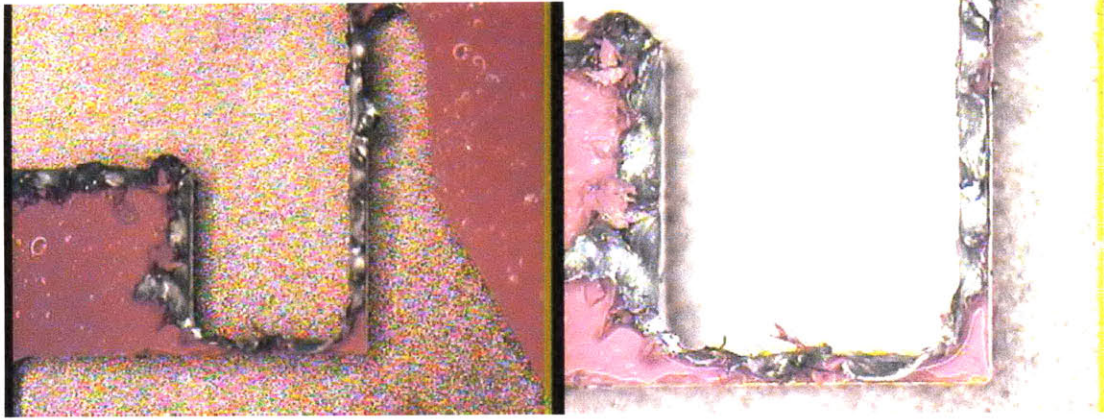
This section summarizes the results of the machining process using visual observation, microscopy and white-light interferometry to investigate part integrity and surface finish. Additionally, suggestions are given to optimize the machining process based on these observations.



**Figure 16:** (a) HexFlex machined from Al 6061-T6 (includes **Process 1**, initial facing operation) (b) HexFlex machined from Al 1100 shim stock already at the specified thickness (400  $\mu\text{m}$ )

### 6.1 *Use of Coolant*

Use of cutting fluid is highly recommended in microscale operations, as it is generally advantageous with regards to surface finish and facilitates chip removal from the cutting area [7]. Empirical evidence shows that cutting fluid is absolutely instrumental in upholding surface integrity while machining HexFlex devices. A sample HexFlex profile was machined without continuous cutting fluid application, and a picture of the resulting part is shown in Figure 17. As Figure 17 illustrates, the surface finish suffered dramatically; this is likely due to either insufficient heat removal from the cutting area or interference of chips that were not removed from the cutting area.

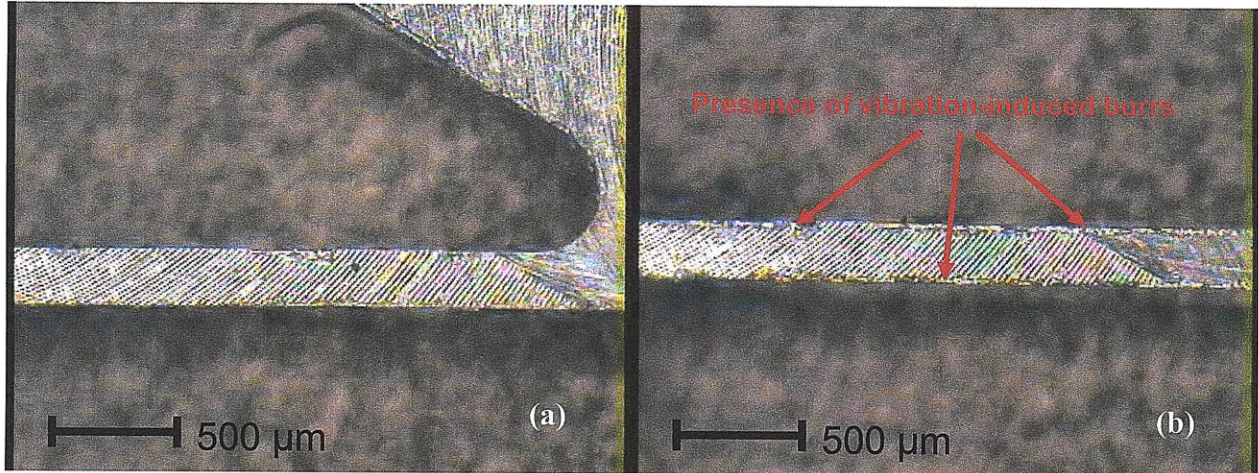


**Figure 17:** Microscopic images of HexFlex machined without liquid coolant.

If available, fluid coolant is greatly preferred over air coolant. The convective heat transfer coefficient for water-based coolants is  $\sim 100$  times greater than that of air, thus greatly expediting heat removal from the cutting area. With respect to tool life, dramatic thermal gradients induced on the cutting edge during the cutting process result in residual stresses that adversely affect the life of the tool. This phenomenon is even more pronounced with smaller tools, as much higher cutting speeds create significant thermal gradients ( $\sim \Delta 100$  Celsius) that conduct much more quickly throughout the tool flank due to small tool cross-sections. It has been observed during this research that lack of water-based coolant leads to premature tool failure during machining operations that normally run smoothly in the presence of liquid coolant. Cutting fluid helps to mediate dramatic temperature gradients at the cutting edge, thus extending tool life.

## 6.2 *Effects of Vibration*

Figures 18(a) and 18(b) show microscopic images of the HexFlex machined from 6061-T6 Aluminum stock. The left picture shows a flexural blade close to its connection point with the base, and the picture on the right shows the same blade far away from its connection point where blade stiffness is significantly less. The presence of vibration-induced surface roughness is clearly visible in the picture on the right, as the resistance of the blade to deflection decreases on the order of  $l^3$  the further away from the base the tool moves.



**Figure 18:** (a) Microscopic image of flexural blade near its connection point with the body, (b) image of same blade far away from the connection point, showing evidence of vibration-induced surface roughness

Steps may be taken to reduce the vibratory effects on these thin blades. A stronger adhesive, such as a glue/solvent combination, may be used in lieu of double-sided tape to substantially increase the shear resistance to deformation at the blade-adhesive interface. Additionally, the radial depth of cut and feed rate on the interior contours may be reduced during finishing operations to decrease the normal component of the cutting force inducing these vibrations.

Removing the flexure from the adhesive tape after machining has completed may lead to unintentional yielding of the thin features. This is another reason it might be beneficial to investigate liquid adhesive/solvent solutions in order to provide a non-stressful way to remove the finished part from the adhesive once machining has finished.

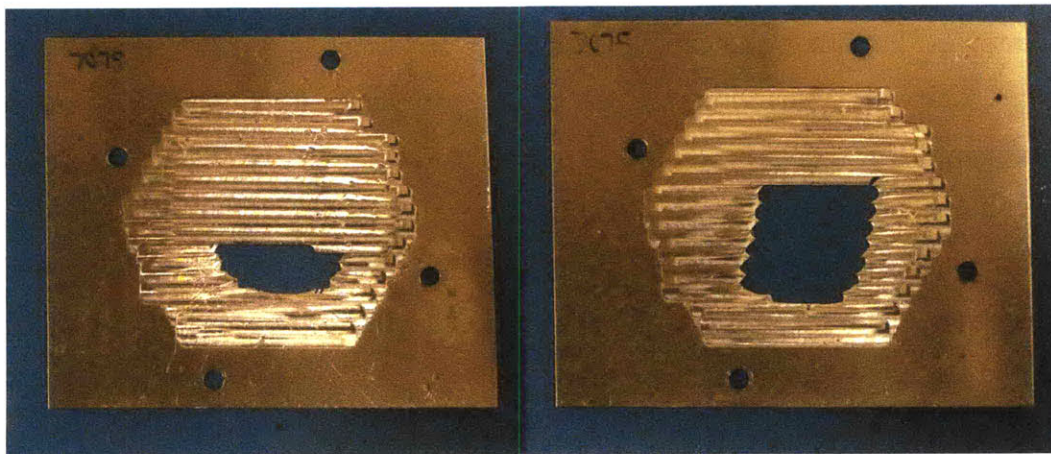
### 6.3 Fixturing

As was mentioned earlier, the design of the available pallets for the Microvolution micromill leads to non-trivialities with respect to part fixturing. The current fixturing method, the sacrificial part with four threaded holes, is sufficient for proof-of-feasibility efforts but surely warrants improvement; the pre-machining of the raw stock results in valuable time losses. Additionally, the sacrificial part was machined using a conventional mill, and the thickness tolerance is  $\pm 0.001''$ . Any deviation in the sacrificial part's thickness directly translates to thickness



deviations in the machined part, and this deviation may become unacceptable when scaling down to parts that are ~10 microns thick.

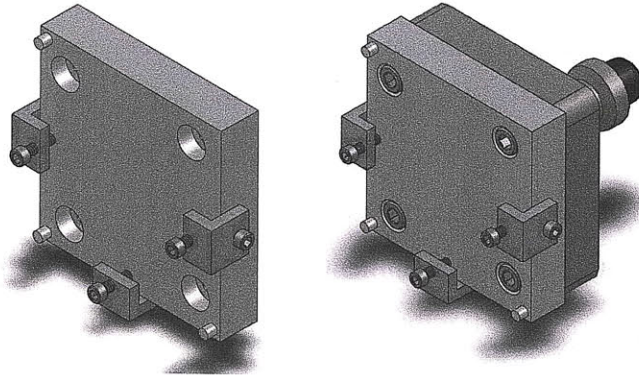
Another observation concerns adhesive application. If double-sided tape is being used as the adhesive of choice to prevent small member deflections, the tape must be applied uniformly across the entire face of the pallet to ensure a relatively flat planar surface upon which the stock is fastened. When tape was localized to the center of the pallet only, tightening down the 4-40 periphery screws caused the stock to “bow up” in the center due to the non-negligible thickness of the adhesive. This caused detachment of the stock from the adhesive during the machining process when coolant is introduced. Detachment resulted in cutting depth variability because the top-of-stock plane was no longer flat but slightly parabolic with respect to the z-direction. During facing operations, this resulted in a web shearing phenomenon where cutting forces impose a state of shear that locally yields the workpiece at a minimum web thickness towards the center of the stock. Pictures of this phenomenon may be seen in Figure 19.



**Figure 19:** Web shearing phenomenon during initial facing operation as a result of stock “bowing” due to clamping action of periphery screws versus non-negligible thickness of centrally-located adhesive.

A recommendation for process improvement is to design a fixture capable of kinematically locating the stock with respect to the x and y zeroes of the mill. Instead of threaded holes, mini clamps should be used so that the stock requires minimal pre-machining prior to fixturing. Finally, this fixture should be face-machined in the micromill to ensure a machining surface

parallel to the z-plane of the micromill to eliminate any angular planar errors that will invariably lead to deviations in part thickness. A solid model of a proposed solution is shown in Figure 20.



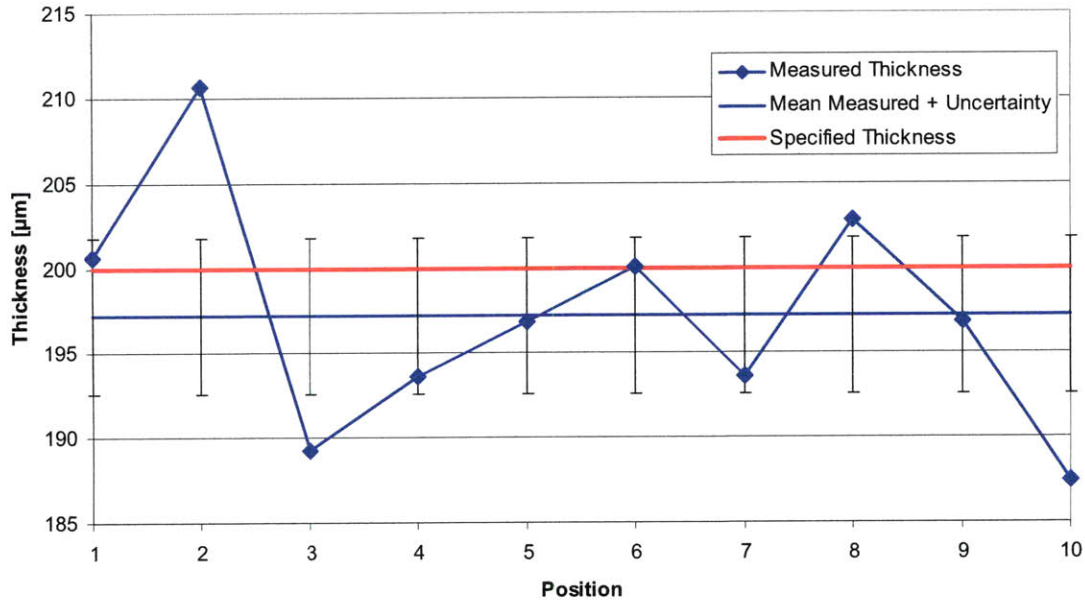
**Figure 20:** Proposed fixturing system, with kinematically-locating pegs and screw clamps.

Three steel pegs lie on the periphery to kinematically locate the stock. Although not necessary for HexFlex, as all machining processes are performed without removing the part from the fixture, a kinematic system might be useful if a part necessitates removal and replacement during machining. Threaded L-brackets with 4-40 screws are used to clamp the stock down onto the fixture after an adhesive has been applied to the surface of the fixture. The top plane is left unobstructed to provide clearance for the tool calibration laser. This solution obviates the need to pre-drill holes into the raw stock, although the stock must still be cut down to size so that it fits within the fixture.

#### 6.4 *Dimensional Precision*

In order to quantify the precision with which the micromill machined the thin flexural beams, microscopic images of the HexFlex devices were taken and analyzed in LabView. Blade thickness was measured at ten unique locations, and uncertainty was calculated with 95% confidence using statistical methods. The specified thickness of the thin blades is 200  $\mu\text{m}$ , and the measured mean thickness of the blades on the machined HexFlex is  $197 \pm 4.62 \mu\text{m}$ . Referring to the spec sheet in Appendix B (Figure B-1), the mill has a positional accuracy of  $\pm 2 \mu\text{m}$ , which is less than the deviation observed empirically. This is an encouraging result, as it means that the end mill wasn't disengaging during finishing contour passes as a result of blade deflection or

vibration. Figure 21 shows a graphical representation of measured vs. ideal blade thicknesses (including calculated uncertainty).



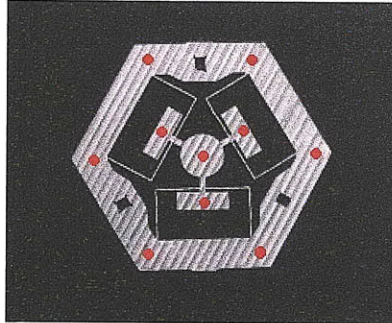
**Figure 21:** Run chart of measured blade thickness. Sample size = 10, Mean = 197 μm, St. Dev. = 6.46 μm, Uncertainty = ± 4.62 μm.

It is also possible that the tool runout adversely affected precision. There is no way to dial in the tool on the micromill, as the tool is clamped using pressurized air; as a result, any runout errors simply have to be tolerated. Visual inspection determined that runout was most likely negligible (at least imperceptible to the unaided eye). Given the measured deviation from specified dimensions, a designer should expect to achieve tolerances as low as  $\pm 3 \mu\text{m}$  when machining parts from the micromill.

### 6.5 Surface Roughness Measurements

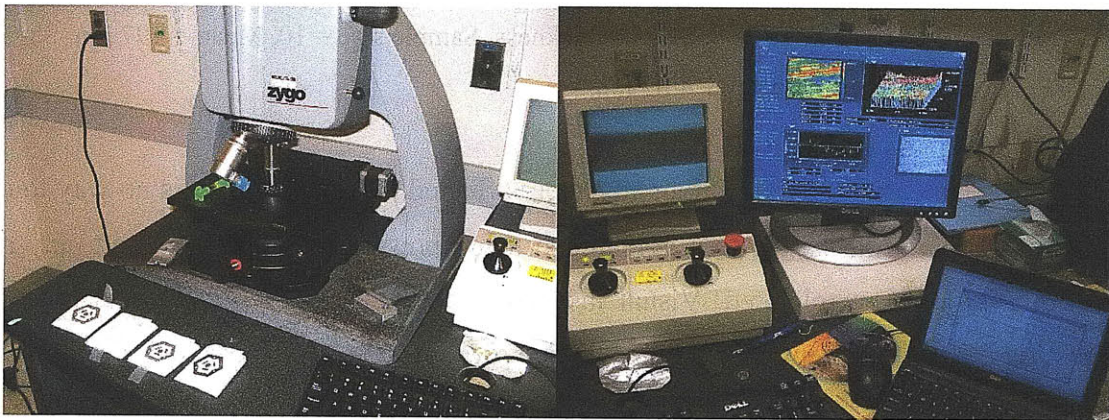
A Zygo white-light interferometer was used to quantify the surface roughness of four different Aluminum 7075 HexFlex devices face-machined with different chip loads. White-light interferometers measure surface roughness by analyzing the fringe patterns of different light wavelengths when reflected from the surface of the measured object.  $270 \mu\text{m} \times 359 \mu\text{m}$

topological areas were imaged at ten discrete locations on each HexFlex in order to obtain a meaningful average of surface roughness, as indicated by Figure 22.



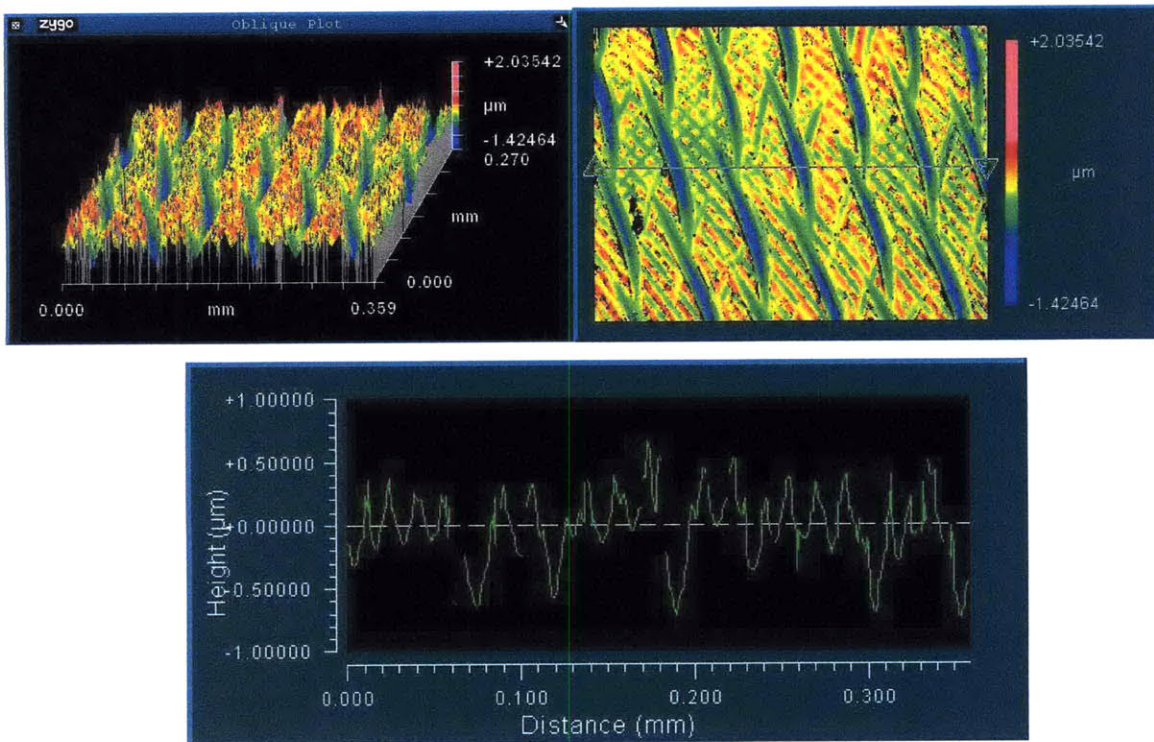
**Figure 22:** Interferometer imaging locations. The intent was to cover a wide spread of the HexFlex surface area for a more comprehensive dataset

The experimental setup is shown below in Figure 23.



**Figure 23:** Experimental setup for white light interferometer measurements.

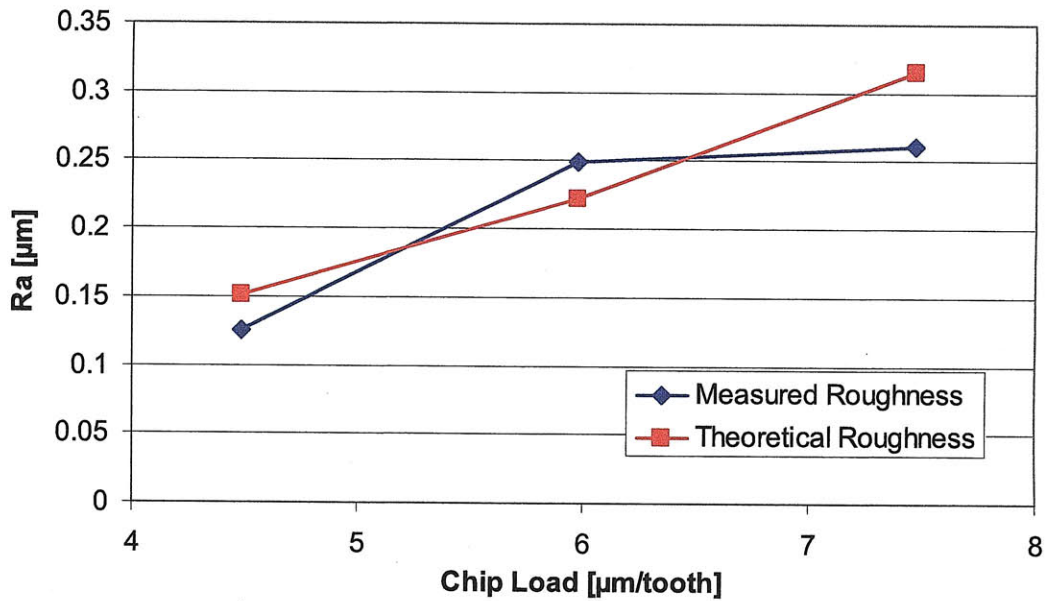
The interferometer's software provided oblique and top-view color-coded topological surface plots, as well as a cross-sectional line plot of the surface (shown in Figure 24) for each image. One may clearly see the methodical repetition of machining lines left over by the cutting edge during the facing operation; the overlapping cutting-edge marks are a result of the radial depth-of-cut being set to half the diameter of the end mill used (for a finer surface finish).



**Figure 24:** Sample surface maps produced by the interferometer

The surface roughness was averaged at each location to obtain a characteristic surface roughness of that particular position. The process was repeated a total of 40 times (10 for each HexFlex), and an average surface roughness was obtained for each HexFlex. Uncertainties were calculated using statistical methods.

Figure 25 shows a comparison of the interferometer measurements with the theoretical polynomial surface roughness fit given in Equation 18 based on chip load. The data points represented are for the 3.175 mm end-mill (Spindle speed = 17,000 RPM) with varying feed rates (254 mm/min, 203 mm/min, and 152 mm/min). A relatively sufficient agreement exists between theoretical values and measured values (from an order of magnitude standpoint).

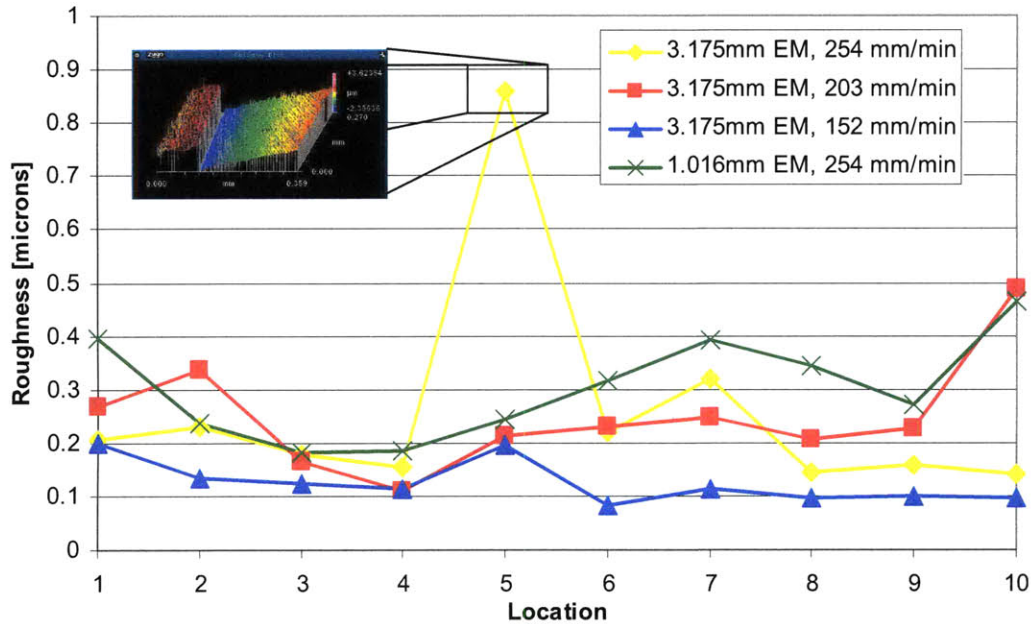


**Figure 25:** Measured surface roughness vs. theoretical surface roughness

Figure 26 gives a run chart of the entire data set, giving an idea of the uncertainty of each measurement and how they scale with each other. Also, the 1.016 mm endmill has been included. The legend calls out the machining parameters for each operation. The best surface finish was  $0.1250 \pm 0.0410 \mu\text{m}$ , achieved with the 3.175 mm endmill at a cutting feed rate of 152 mm/min. It is worth noting that this surface finish is superior to that of uncut stock (which was found to be  $0.2120 \pm 0.0190 \mu\text{m}$ ). An observable trend is that as chip load decreases, surface finish becomes more uniform across the entire part (most likely a result of reduced chatter/vibrations induced by lesser cutting forces).

Surprisingly, the worst surface finish was achieved with the 1.016 mm end mill (spindle speed = 38,000) at a feed rate of 254 mm/min. This process had the lightest chip load and slowest surface speed of all the tests, so the expectation was that it would achieve the best finish. According to Equation 18, the theoretical surface finish is  $0.1100 \mu\text{m}$ , but actual measurements yielded an average surface finish of  $0.3030 \pm 0.0680 \mu\text{m}$  (approximately 175% error). The significant discrepancy may be a result of unfavorable and uncontrollable process alterations (such as adhesive delamination, tool runout, or workpiece vibration). Alternatively, despite the reduced chip load, the tool still may have experienced deflection induced by the cutting force components. The takeaway from these interferometer measurements is that a surface roughness

of less than 300 nm is easily achievable with the micromill. Additionally, as was the case with the 3.175 tool at 152 mm/min feed rate, it is possible to achieve a surface finish superior to that of uncut stock with the micromill. A complete numerical dataset with associated roughness averages, uncertainties and standard deviations is available in the appendices.



**Figure 26:** Measured surface roughness data for four 7075 Al Hexflex devices

### 6.6 The Future: Scaling Down

Now that micromilling has been demonstrated as a feasible means to manufacture mesoscale flexural bodies, there will invariably be incentive to scale the process down to microscale flexures (~1 mm x ~1 mm diameter, micro-thin features). In order to get a feel for the scaling-down capabilities of the micromill, a test part was designed to roughly quantify the minimum feature thickness achievable. A picture of this part is shown in Appendix B (Figure B-3). The part consists of 8 ribs with thicknesses that range from 500  $\mu\text{m}$  to 10  $\mu\text{m}$ . It also features pockets with variable web thickness ranging from 500  $\mu\text{m}$  to 10  $\mu\text{m}$  thick. Three different end mills (3.175 mm, 1.016 mm, and .508 mm) with variable feed rates were used. The process parameters and results are given in Table 2.

**Table 2:** Process parameters for test part designed to quantify minimum rib/web thicknesses achievable with the micromill

	Tool Diameter [ $\mu\text{m}$ ]	Chip Load [ $\mu\text{m}/\text{tooth}$ ]	Minimum Rib Thickness [ $\mu\text{m}$ ]	Minimum Web Thickness [ $\mu\text{m}$ ]
Round 1	3.175	7.50	10	100
Round 2	1.016	3.34	10	100
Round 3	.508	5.29	10	100

With regards to rib thickness, all three processes successfully machined the minimum rib thickness of the part, which was 10  $\mu\text{m}$ . This is a very promising result which lends to the precision of the micromill. In all three cases, webs thinner than 100  $\mu\text{m}$  were sheared off completely due to shear stresses induced by the cutting forces. It is also possible that the deviation in surface flatness of the fixture led to unequal depths of cut, however the machining area was kept relatively small (1 cm x 1 cm) to minimize flatness errors. In the future, more tests with greater variability regarding tool diameter and chip load should be performed in order to amalgamate more data points and produce more accurate results. Regardless, from both a process and a precision standpoint, stock should be purchased at specified design thicknesses for any parts thinner than 100  $\mu\text{m}$ .

## Chapter 7: Conclusion

This research focused on demonstrating the feasibility of using micromilling as a process to manufacture mesoscale nanositioners. The adoption of micromilling at the microdevice level could potentially lower MEMS production costs and open up an entirely new design space with regards to materials selection and process flexibility. It has been demonstrated herein, both through theory and practice, that micromilling is a feasible alternative to traditional microfabrication methods for designers seeking to prototype high-quality and to-spec mesoscale nanositioners in a low-volume environment. Cutting force models were used to generate and validate machining parameters that would avoid tool failure and uphold part integrity. These parameters were employed in the machining of several HexFlex test parts out of various aluminum alloys. Post-machining observations and analyses showed these parts to be within  $\pm 3$   $\mu\text{m}$  of specified dimensions, giving an indication of what a designer should expect as far as



assigning tolerances goes. Additionally, the surface roughness was found to be less than 300 nm in the general case, and as low as 125 nm in the optimum case (superior to that of uncut stock).

### **Future Work:**

In the future, HexFlex devices machined from the micromill should be tested for their flexural response. The response of the micromilled flexure should be correlated with the responses of HexFlex devices fabricated using conventional techniques. Pending the success of these flexural validations, this research could provide a step forward in the design and manufacturing of low-cost prototypical nanopositioners.

In addition, more parametric tests could be performed to determine the absolute optimum machining parameters for micromilling flexures that will minimize machining time and maximize the quality of the product. This research has shown that a logical methodology may be applied to determine baseline cutting parameters with the interest of avoiding tool failure and optimizing surface roughness of the machined product. The variability and dynamism associated with the micromilling process are difficult to model theoretically and should ultimately be verified empirically to determine optimum production conditions.

## References

- [1] Culpepper, M. and Anderson, G., "Design of a Low-Cost Nano-Manipulator Which Utilizes a Monolithic, Spatial Compliant Mechanism." *Precision Engineering*, 2004, Vol. 28. pp. 469-482
- [2] Hopkins, J. and Culpepper, M., "Synthesis of multi-degree of freedom, parallel flexure system concepts via Freedom and Constraint Topology (FACT)." *Precision Engineering*, 2010, Vol. 34. pp. 259-270
- [3] Bao, W.Y., Tansel, I.N., "Modeling Micro-End-Milling Operations, Part I: Analytical Cutting Force Model." *International Journal of Machine Tools & Manufacture*, 2000, Vol. 40. pp 2155-2173
- [4] Perez, H., Vizan, A., Hernandez, J.C., Guzman, M., "Estimation of Cutting Forces in Micromilling through the Determination of Specific Cutting Pressures." *Journal of Materials Processing Technology*, Vol. 190. pp. 18-22
- [5] Ozel, T., Liu, X., Dhanorker, A., "Modelling and Simulation of Micro-Milling Process."
- [6] Popov, K., Dimov, S., Pham, D.T., Ivanov, A., "Micromilling Strategies for Machining Thin Features." *Proc. IMechE*, 2006, Vol. 220. pp 1677-1684
- [7] Ziegert, J. and Pathak, J., "An Ultra-High Speed Spindle for Micro-Milling."
- [8] Dhanorker, A. and Ozel, T., "An Experimental and Modeling Study on Meso/Micro End Milling Process." *ASME*, 2006.
- [9] Shaw, Milton. "Metal Cutting Principles." Oxford University Press, USA; 2 edition: July 8, 2004
- [10] Klock, F., Quito, F., Arntz, K., Souza, A., "A Study of the Influence of Cutting Parameters on Micro Milling of Steel with Cubic Boron Nitride (CBN) Tools." *Micromachining and Microfabrication Process Technology*, 2009, Vol. 14.
- [11] Dimov, S., Pham, D.T., Ivanov, A., Popov, K., Fansen, K., "Micromilling Strategies: Optimization Issues." *Proc. Instn. Mech. Engrs*, 2004, Vol. 218. pp 731-736
- [12] Kim, C.J., Mayor, J.R. and Ni, J. "A static model of chip formation in microscale milling", *ASME Journal of Manufacturing Science and Engineering*, 2004, Vol. 126, pp.710-718.
- [13] Lee, K. and Dornfeld, D.A. "Micro-burr formation and minimization through process control." *Precision Engineering*, 2005, Vol. 29. pp. 246-252

## Appendix A

Appendix A contains the MathCAD model (showing relevant equations) used to calculate toolpiece factors-of-safety based on user-selected cutting parameters.

### Micromill Machine Parameter Selection

This model calculates relevant factors of safety (FOS) for the toolpiece given cutting parameters as inputs. Both immediate FOS and fatigue-driven FOS are given. Additionally, theoretical surface roughness is calculated based on the polynomial model developed by Lee.

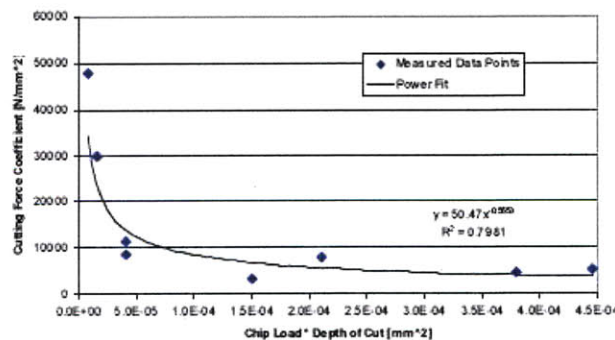
#### Tool Properties

$d_{\text{tool}} := .5\text{mm}$	Diameter of the tool
$l_{\text{flute}} := 3 \cdot d_{\text{tool}}$	Flute length
$\sigma_y := 1.3\text{GPa}$	Yield Stress
$Z := 2$	Number of Flutes
$K_s := 2$	Stress concentration factor
$d_{\text{effective}} := 0.8 \cdot d_{\text{tool}}$	Effective Diameter
$I_{\text{tool}} := \frac{\pi \cdot \left(\frac{d_{\text{effective}}}{2}\right)^4}{4}$	Second moment of area of tool
$S_e := 689\text{MPa}$	Endurance Strength of Tool
$S_{\text{ut}} := 1.51\text{GPa}$	Ultimate Tensile Strength of Tool
$S_{\text{uc}} := 5.24\text{GPa}$	Ultimate Compressive Strength of Tool

#### Process Parameters

$\text{RPM} := 48000 \frac{1}{\text{min}}$	Spindle Speed (RPM)
$f_c := 1000 \frac{\text{mm}}{\text{min}}$	Cutting Feed
$d_{\text{axial}} := .05\text{mm}$	Axial Depth of Cut
$d_{\text{radial}} := .5\text{mm}$	Radial Depth of Cut
$f_t := \frac{f_c}{(\text{RPM} \cdot Z)}$	Chip load (or feed per tooth)
$v_c := \frac{\text{RPM} \cdot d_{\text{tool}} \cdot 2\pi}{2}$	Surface speed

**\*\*NOTE:** these are all typical values for tungsten carbide tool steel



#### Workpiece Properties

$$K_m := 50.47 \cdot \left[ \left( \frac{f_t}{\text{mm}} \cdot \frac{d_{\text{axial}}}{\text{mm}} \right)^{-0.5553} \right] \frac{\text{N}}{\text{mm}^2}$$

Material coefficient for Aluminum 6061-T6 (based on empirical data shown in above graph)

$$\tau_{\text{ywp}} := 287\text{MPa}$$

Shear strength of workpiece

$$\tau_{\text{y6061}} := 207\text{MPa}$$

Shear strength of 6061-T6 Aluminum (material about which cutting forces estimates are normalized)

## Cutting Force Calculations

$$F_{\text{feed}} := \left( \frac{\tau_{\text{ywp}}}{\tau_{\text{y6061}}} \right) \cdot K_m \cdot f_t \cdot d_{\text{axial}}$$

Feed cutting force based on previously-determined material coefficient

$$F_{\text{normal}} := F_{\text{feed}} \cdot 0.8$$

Normal cutting force (Approximately)

## Toolpiece Stress Calculations

$$\sigma_{\text{bend}} := \frac{\left( \frac{d_{\text{effective}}}{2} \right) \cdot F_{\text{feed}} \cdot l_{\text{flute}}}{I_{\text{tool}}}$$

$$\tau_{\text{torsion}} := \frac{8F_{\text{feed}}}{\pi \cdot d_{\text{effective}}^2}$$

Characteristic bending, torsional, and shear stresses imparted on tool by cutting forces.

$$\tau_{\text{fshear}} := \frac{16 \cdot F_{\text{feed}}}{3 \cdot \pi \cdot d_{\text{effective}}^2}$$

$$\tau_{\text{nshear}} := \frac{16 \cdot F_{\text{normal}}}{3 \cdot \pi \cdot d_{\text{effective}}^2}$$

$$\sigma_{\text{tensor}} := \begin{pmatrix} 0 & \tau_{\text{torsion}} & \tau_{\text{nshear}} \\ \tau_{\text{torsion}} & 0 & \tau_{\text{fshear}} \\ \tau_{\text{nshear}} & \tau_{\text{fshear}} & \sigma_{\text{bend}} \end{pmatrix}$$

Stress tensor and invariant constants for material element

$$I_1 := \frac{\sigma_{\text{bend}}}{\text{GPa}}$$

$$I_2 := \frac{\tau_{\text{fshear}}^2 + \tau_{\text{nshear}}^2 + \tau_{\text{torsion}}^2}{\text{GPa}^2}$$

Stress Invariants

$$I_3 := \frac{2 \cdot \tau_{\text{torsion}} \cdot \tau_{\text{fshear}} \cdot \tau_{\text{nshear}} - \sigma_{\text{bend}} \cdot \tau_{\text{torsion}}^2}{\text{GPa}^3}$$

$$\sigma^3 - I_1 \cdot \sigma^2 + I_2 \cdot \sigma - I_3 = 0 \quad \text{Cubic invariant equation}$$

$$v := \begin{pmatrix} -I_3 \\ I_2 \\ I_1 \\ 1 \end{pmatrix} \quad \text{Vector of Coefficients}$$

$$\text{root1} := \text{polyroots}(v)_{0,0}$$

$$\text{root2} := \text{polyroots}(v)_{1,0}$$

$$\text{root3} := \text{polyroots}(v)_{2,0}$$

Roots of the polynomial equation (principal stresses)

$$\text{roots} := \begin{pmatrix} \text{root1} \\ \text{root2} \\ \text{root3} \end{pmatrix} \quad \text{Vector with roots of cubic equation}$$

$$\sigma_1 := \max(\text{roots}) \cdot \text{GPa}$$

Maximum and minimum principal stresses for current loading situation

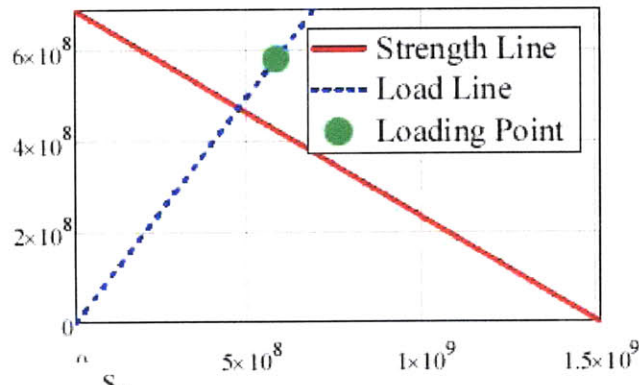
$$\sigma_2 := \min(\text{polyroots}(v)) \cdot \text{GPa}$$

## Factors of Safety, Failure Calculations

$$\text{Mohr} := \frac{\sigma_1}{S_{ut}} - \frac{\sigma_2}{S_{uc}} \quad \text{Mohr criterion for brittle failure}$$

$$\text{FOS}_{\text{immediate}} := \frac{1}{\text{Mohr} \cdot K_s} \quad \text{Factor of safety for immediate tool yield}$$

$$\text{Strengthline}(x) := \frac{-S_e}{S_{ut}}x + S_e \quad \sigma_a := \frac{K_s \cdot \sigma_1}{2} \quad \sigma_m := \frac{K_s \cdot \sigma_1}{2} \quad \text{Loadline}(x) := x$$



Goodman diagram for cyclic loading. Area beneath strength line is safe zone

$$\text{FOS}_{\text{fatigue}} := \frac{S_e}{K_s \cdot \sigma_1} \quad \text{Factor of safety for fatigue-driven yield}$$

$$b_{\text{fatigue}} := \frac{-\left(\log\left(\frac{0.9 \cdot \sigma_y}{\text{GPa}}\right) - \log\left(\frac{S_e}{\text{GPa}}\right)\right)}{\log(10^6) - \log(10^3)}$$

Characteristic slope of S-N diagram (Approximated from general fatigue curve of steel)

$$N_{\text{failure}} := (10^6) \cdot \left(\frac{\sigma_1}{S_e}\right)^{\left(\frac{1}{b_{\text{fatigue}}}\right)}$$

Approximate loading cycles to failure

$$\text{distance}_{\text{failure}} := N_{\text{failure}} \cdot f_t \left[0.5 \cdot \left(\frac{d_{\text{tool}}}{d_{\text{radial}}}\right)\right]$$

Approximate distance traveled until failure

$$\text{MRR}_{\text{failure}} := \text{distance}_{\text{failure}} \cdot d_{\text{axial}} \cdot d_{\text{tool}}$$

Approximate material volume removed before tool failure

$$\text{FOS}_{\text{immediate}} = 1.275$$

Factor of Safety for immediate failure

$$\text{FOS}_{\text{fatigue}} = 0.593$$

Factor of Safety for fatigue

$$\text{distance}_{\text{failure}} = 48.018 \text{ m}$$

Distance travelled by tool until failure

$$R_a := \frac{1}{10} \left( 43.6 + \frac{43.9}{\text{m}} \cdot f_t + \frac{46.3}{\text{m}^2} \cdot f_t^2 + \frac{1256}{\text{m}} \cdot v_c - \frac{990}{\text{m}^2} \cdot f_t \cdot v_c \right) \quad \text{Surface roughness polynomial fit based on research performed by Lee}$$

$$R_a = 162.193$$

Surface Roughness (in nanometers)

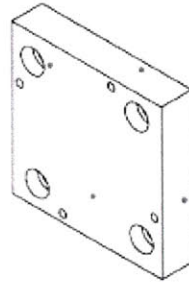
## Appendix B

Appendix B contains the mill spec sheet, sacrificial part drawing, and the raw results of post-machining testing and validation.

<b>Positioning Accuracy:</b>	0.00008" (2 microns)
<b>Repeatability:</b>	0.000008" (0.2 microns)
<b>Resolution:</b>	0.0000019" (0.05 microns)
<b>Automatic Tool Changer:</b>	36 pocket Automatic Tool Changer (ATC) supporting tools ranging in diameter from 0.002" - 0.125".
<b>Working Volume:</b>	X: 2.48" (63mm); Y: 2.48" (63mm); Z: 2.48" (63mm)
<b>Maximum Acceleration:</b>	5G
<b>Spindle options including:</b>	Electrically driven spindle featuring a maximum speed of 40,000rpm and automatic-collet based tool changing system Air-bearing, electrically driven spindle featuring a maximum speed of 80,000rpm Air-bearing, air-turbine driven NSK spindle featuring a maximum speed of 160,000rpm
<b>Utility Requirement:</b>	Air - 100 PSI, 6CFM; Electricity - 120VAC, 20A
<b>Advanced Mounting System:</b>	Quick-change, high-repeatability workpiece and spindle mount system
<b>Machine Features:</b>	AC linear motors on X, Y and Z stages Heidenhain linear optical encoders on X, Y and Z stages Precision granite support structures High-performance, open-architecture CNC controller

**Figure B-1:** Spec sheet of Microlution 363-S 3-axis horizontal micro-milling machine

Material: Aluminum 6061-T6  
Stock: 3/8" Plate  
Units: Inches

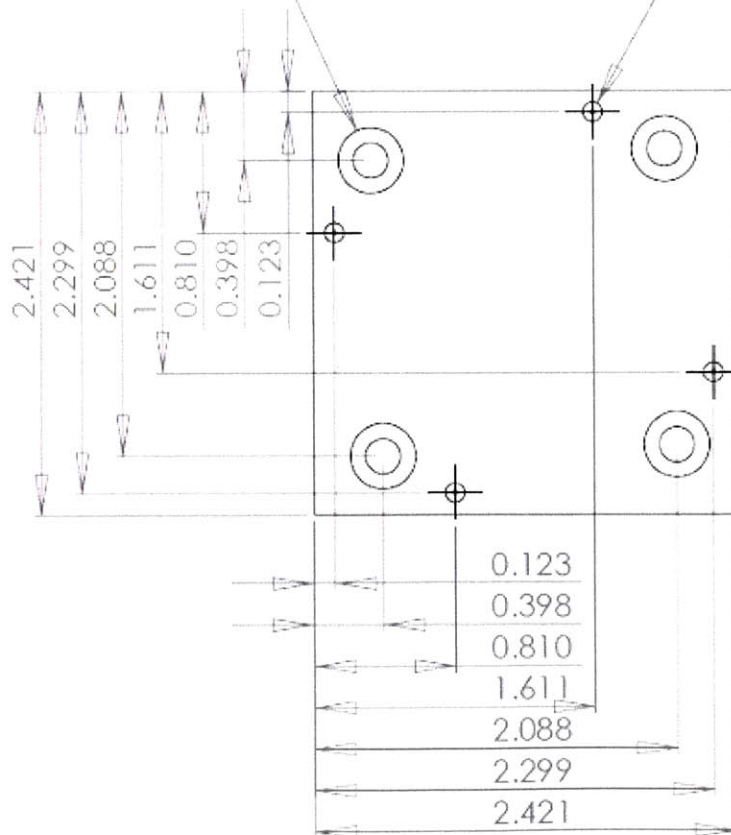


### Sacrificial Part

1: Cut to spec, face mill re  
2: Drill and Tap Holes

4 x  $\varnothing$  0.201 THRU ALL  
 $\square$   $\varnothing$  0.375  $\nabla$  0.190  
10-32 Thru Hole, C-Bore  
Hole: # 7 Drill  
C-Bore: 5/16" EM

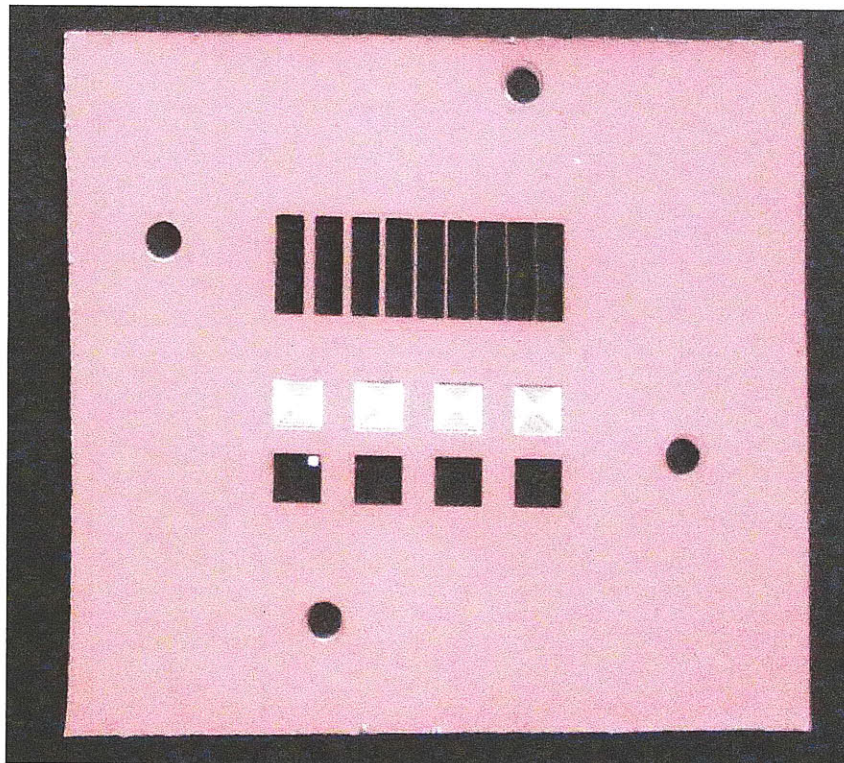
4 x  $\varnothing$  0.089 THRU ALL  
4-40 UNC THRU ALL  
4-40 Threaded hole (from back)  
Hole: # 43 Drill



1:1

**Table B-1:** Measurements of blade thickness

Position	Measured [ $\mu\text{m}$ ]	Specified [ $\mu\text{m}$ ]	Error
1	200.6	200	0.32%
2	210.7	200	5.33%
3	189.2	200	5.38%
4	193.6	200	3.20%
5	196.9	200	1.57%
6	200.0	200	0.01%
7	193.6	200	3.21%
8	202.8	200	1.40%
9	196.9	200	1.57%
10	187.4	200	6.29%
	<b>Measured Avg.</b>	<b>197.2</b>	
	<b>St. Dev.</b>	<b>6.464</b>	
	<b>Uncertainty</b>	<b><math>\pm 4.624</math></b>	



**Figure B-3:** Test part for roughly quantifying minimum blade and web thickness. Blade thicknesses and web thicknesses range from 500  $\mu\text{m}$  to 10  $\mu\text{m}$



**Table B-2:** White-light interferometer surface roughness measurements

<b>Location</b>	<b>Ra (1)</b>	<b>Ra (2)</b>	<b>Ra (3)</b>	<b>Ra(4)</b>	<b>Uncut</b>
1	0.206	0.267	0.199	0.394	0.245
2	0.231	0.337	0.135	0.237	0.229
3	0.177	0.166	0.124	0.181	0.214
4	0.153	0.110	0.114	0.187	0.194
5	0.858	0.213	0.196	0.245	0.207
6	0.219	0.230	0.081	0.315	0.214
7	0.319	0.247	0.115	0.391	0.175
8	0.143	0.205	0.097	0.344	0.217
9	0.158	0.227	0.098	0.272	0.203
10	0.140	0.489	0.096	0.463	0.223
<b>Average</b>	0.260	0.249	0.126	0.303	0.212
<b>St.Dev</b>	0.217	0.103	0.041	0.095	0.019
<b>95% Uncertainty</b>	0.155	0.074	0.029	0.068	0.014
<b>Theoretical</b>	0.315	0.222	0.151	0.110	N/A
<b>Error</b>	17.2%	12.0%	16.9%	175.2%	N/A